Electronic Supplementary Material (ESI) for Environmental Science: Atmospheres.
This journal is © The Royal Society of Chemistry 2022

Seasonality of isoprene emissions and oxidation products above the remote Amazon

B. Langford, E. House, A. Valach, C. N. Hewitt, P. Artaxo, M. P. Barkley, J. Brito, E. Carnell, B. Davison, A. R. MacKenzie, E. A. Marais, M. J. Newland, A. R. Rickard, M. D. Shaw, A. M. Yáñez-Serrano, and E. Nemitz

Supporting Information

1. Measurements

1.1 Measurement site and climate

Measurements of volatile organic compound (VOC) concentrations and fluxes were made above the Amazon rainforest from September 2013 to July 2014. Sample air was drawn from an inlet mounted at a height of 38 m on the triangular tower TT34 at the LBA ZF2 measurement site (2.594637° S, 60.209519° W, altitude 67 m) located in the Reserva Biologica do Cueiras in Central Amazonia, Brazil. The tower is surrounded by undisturbed, mature, *terra firme* tropical rainforest with a canopy height of between 25-35 m and a single-sided leaf area index (LAI) of 4.3-6.5 m^2 m^{-2}(1).

The ZF2 site in central Amazonia is located in an equatorial rainforest with high precipitation (average annual rainfall around 3000 mm). Climatologically, there is a prolonged wet season from November to June, peaking in February and March (precipitation of 250 mm to 350 mm per month), and a short dry season (precipitation around 60 mm per month) in July to October(2). However, there is considerable year-to-year variability in timing and actual precipitation of the wet and dry seasons. The mean monthly relative humidity ranges between 72% (October) and 86% (March). The high annual precipitation and humidity is associated with low level convergence of moist air flowing from the east, as well as high rates of evapotranspiration, which recycles up to 30% of precipitation(3). Generally, the sea surface temperature of the tropical Atlantic to the east and the forcing produced by the Andes to the west are linked to the monsoon system, which is the main driver of precipitation across the Amazon basin(4).

Measurements at the ZF2 site showed average temperatures of 25 ± 2.7 °C peaking at the end of the dry season in October (27 °C) and midday median (and interquartile range, IQR) photosynthetically active radiation (PAR) of 930 (374 – 1430) µmol m^{-2} s^{-1}, which was highest during the dry season, peaking in September. The years 2013 and 2014 exhibited less pronounced seasonality compared with the 1999-2012 average, with more precipitation during the dry season and less in the wet season (E. Alves, personal communication, 2015)(5, 6). In particular, November 2013 was cooler and wetter than average, whereas April 2014 was warmer and drier than the long term mean. This means the meteorologically induced seasonality observed in the results from this study may be attenuated compared with the long-term mean behaviour. The mean ambient pressure was 997 ± 5.6 mbar with low average wind speeds of 1.9 ± 0.9 m s^{-1} (at 38 m above ground) from mostly easterly directions, i.e. trade winds from the equatorial Atlantic (52% frequency and monthly median directions between 84° and 144°).

The vegetation at the ZF2 site consists of evergreen broadleaf trees growing on well-drained, nutrient-poor yellow clay oxisols. The landscape, whilst overall very flat, is marked by lowlands interspersed by small plateaux ranging from 50 m to 110 m altitude with dense tall trees on the plateaux where the tower is located, and open palm forests in the valley bottoms(7). The surrounding features of the reserve include a highway (BR-174) 20 km to the east, which is the only paved land connection to Manaus (from Venezuela in the North), and the Cuieiras river, which is a tributary to the Rio Negro, 13 km to the west. There are narrow strips of fragmented clearings through the forest, representing mosaic agriculture with degraded vegetation, 12 km to the south and 18 km to the north of the site. The plateau area around the tower and the reserve itself is very representative of undisturbed primary rainforest in central Amazonia(8, 9).

1.2 Instrumentation and Data Acquisition

A high sensitivity proton transfer reaction - (quadrupole) mass spectrometer (PTR-MS) (Ionicon Analytik GmbH, Innsbruck, Austria) was deployed to measure volatile organic compound mixing ratios and eddy covariance flux measurements at TT34 from the 1 September 2013 to 20 July 2014 and a total of 4951 hours of fast-response concentration measurements were made. Air was sampled at ~80 L min^{-1} through a 1/2” OD (95 mm ID) PFA (PFA-T8-062-100, Swagelok) sampling tube with the inlet located ~100 mm below a sonic anemometer (Model R3-50, Gill Instruments, UK) operated in axis mode at 10 Hz at the top of the tower at a height of 38.5 m . This high flowrate ensured there was turbulent flow within the tube (Re ≈ 9600) to limit attenuation of the measured fluxes. The sampling tube was insulated and heated to 40 ˚C inside the air conditioned cabin, in which the PTR-MS was housed at the bottom of the tower, and for the first 2 m up the tower to prevent condensation occurring. The PTR-MS was operated with a drift tube temperature of 50 ˚C, pressure of 2.0 mbar and a voltage of 550 V (drift tube length ca. 9.5 cm) with a resultant E/N (E, electric field strength, N, buffer gas number density) of ~ 130 Td (1 Td = 10^{-17} V cm^2), which was maintained throughout the measurement period. The ion source current was 6.0 mA and the water flow rate was 6-8 sccm. The campaign average of the mean counts per second (cps) for the mass-to-charge ratio (m/z) of the first water cluster $H_3O^+(H_2O)$ (m/z 37) as a percentage of the cps of the primary ion (m/z 19) while recording in multiple ion detection (MID) mode was 3.4% (SD 0.4%, n = 4930). O_2^+ counts were <0.40% and NO^+ cps <0.15% of m/z 19 cps throughout the campaign as determined from periodic mass scan measurements.

During flux acquisition mode the PTR-MS sequentially sampled a total of ten mass-to-charge ratios which included the primary ion, measured at the isotopologue ($H_3{}^{18}O^+$) at *m/z* 21, as well as the first water cluster ($H_3O^+ \cdot H_2O^+$, *m/z* 37), isoprene (*m/z* 69),isoprene oxidation products (*m/z* 71), acetonitrile (*m/z* 42), plus an additional six *m/z* which are not considered in this analysis. The signals detected at *m/z* 69 were ascribed to isoprene plus any furan⁽¹⁰⁾ or fragments of -methyl-3-butene-2-ol (MBO) present whereas the ion counts at *m/z* 71 were attributed to the isobaric compounds methyl-vinyl-ketone (MVK) and methacrolein (MACR) (both C_4H_6O) as well as a contribution from isoprene hydroxy hydroperoxides (ISOPOOH). While ISOPOOH ($C_5H_{10}O_3$) has a higher molecular weight and would be expected to be detected at *m/z* 119, Rivera-Rios et al. (2014)⁽¹¹⁾ demonstrated that upon contact with the hot metal surfaces inside the PTR-MS ISOPOOH loses a peroxy radical with the major fragment ion then presenting at *m/z* 71 and indistinguishable from MVK+MACR with a PTR-MS instrument. The suite of selected masses were measured in MID mode with a dwell time of 0.2 s per *m/z* with the exception of *m/z* 21 and *m/z* 37 which were both measured with a 0.1 s, which resulted in a total measurement cycle of 2 s. The flux mode acquisition lasted for 45 minutes which provided 1350 disjunct data points for the flux calculation per averaging period.

The instrument background was assessed for five minutes of each hour by sampling zero air from a commercial platinum alumina-based zero air generator (Model 75-83-220, Parker Balston) in a mass scan mode. The five minute average background mixing ratio was subtracted from the ambient mixing ratio measurements of the corresponding hour. When no background measurement was available for a given hour, the median of the hourly backgrounds measured in the same month was applied. The mixing ratio limit of detection (LoD) was approximated from two standard deviations of the five min background measurement (in normalised counts per second, ncps) for a given hour divided by the corresponding sensitivity (ncps ppbv^{-1}). Here normalised cps refers to normalisation to H_3O^+ of 10^6 cps and a drift tube pressure of 2.0 mbar. Ensemble averages of the applied background and LoD mixing ratios are given in Table 1, together with average sensitivities. Fluxes and mixing ratios below the LoD were included in the analysis of averaged data, as their removal can cause a bias towards high values, because when measurements are below the LoD they are indeed small⁽¹²⁾. Methods to substitute periods of data <LoD are available; however, these have also been shown to result in a significant bias, either high or low depending on the values used⁽¹³⁾. The percentage and number of data points which fail the LoD are given in Table S1.

Table S1. Ensemble averages of hourly applied sensitivities, background mixing ratios and limits of detection (LoD). Normalised counts s^{-1} (ncps) refer to raw counts s^{-1} normalised to 10^6 cps H_3O^+ and drift tube pressure of 2.0 mbar. Mixing ratio LoDs were approximated from two standard deviations of hourly (5 min) background ncps divided by measured sensitivities (ncps $ppbv^{-1}$). The percentage and number of hours in which the mixing ratios measured in MID mode were below the LoD is shown.

	Sensitivity[a] *(ncps ppbv^{-1})* *Median (IQR)*	*Background (ppbv)* *Median (IQR)*	*LoD (ppbv)* *Median (IQR)*	*% of values <LoD (n)*
Isoprene (m/z 69)	3.78 (0.35)	0.16 (0.11)	0.50 (0.17)	13 (644)
MVK+MACR+ ISOPOOH product ions (m/z 71)	12.02 (2.08)	0.08 (0.07)	0.23 (0.11)	22 (1066)

[a] average sensitivity and uncertainties for VOC mixing ratios were 20-30%, depending on compound.

Sensitivities for the compounds detected by PTR-MS were determined from automated calibrations performed from the end of October 2013 onward using a gravimetrically prepared standard containing 15 VOCs which included both isoprene and MVK, in ultrahigh purity nitrogen (Apel Riemer Environmental Inc., Boulder, CO, USA) diluted with dry zero air. A mass flow controller (MKS Instruments Limited, model 1259C; range 0.015 to 1 standard L min^{-1}) was used to control the zero air dilution flow and was automatically calibrated prior to each multipoint calibration using an electronic mass flow meter (model MAS1009AV2, Kobold). A further mass flow controller with 316 grade stainless steel body (model F-200DV-AAD-22-V, range 0-15 standard mL min^{-1}, Bronkhorst, Ruurlo, The Netherlands) was used to control the VOC flow and was manually calibrated at regular intervals against a mini-Buck flow calibrator (mini-Buck calibrator model M-5, A-P Buck, USA).

Multipoint calibrations in which selected *m/z* were monitored at the dwell times employed in MID mode were interleaved by single-point calibrations undertaken in scan mode. To check for memory effects, multipoint calibrations were performed up and down the concentration range. Mixing ratios of isoprene and MVK sampled during calibrations were in the range of 2 to 20 ppbv each. Zero air measurements were performed before and after sampling at each VOC concentration. The secondary electron multiplier (SEM) voltage of the PTR-MS was optimised prior to calibrations. Calibrations were scheduled during the night when concentrations were low and when turbulence was often insufficient for robust flux quantification. Humidified calibrations using either a bubbler or a dewpoint generator (Model LI610, LI-COR, Lincoln, Nebraska, USA) were performed off-line. A T/RH probe (HMP60, Vaisala, Helsinki, Finland) in the excess flow was used to monitor relative humidity and temperature. Humidity dependent sensitivities were applied to *m/z* 69 and *m/z* 71 in a method analogous to that described by Inomata et al.(14) and Kameyama et al.(15-17).

1.3 Flux measurement time-lag assessment

A prescribed time lag of 8.5 s was applied to the isoprene data and 9 s was used for Iso_{ox} data. This time-lag (Δt) was determined from analysis of the histogram of time-lags determined from the maximum in the cross-covariance of the isoprene concentration and vertical wind velocity (MAX method) following the recommendations of Langford et al. (2015)(18). Figure S1 shows the histograms of isoprene (red) and Iso_{ox} (MVK+MACR+ISOPOOH, green) which showed remarkable consistency throughout the 11 month measurement period. The peak of the histogram is broader for the isoprene oxidation products which reflects the lower signal to noise ratio for this compound relative to isoprene which was observed at much higher concentrations. Once the peaks in the MAX time-lag histogram were calculated the fluxes were all reprocessed with the prescribed time-lags stated above.

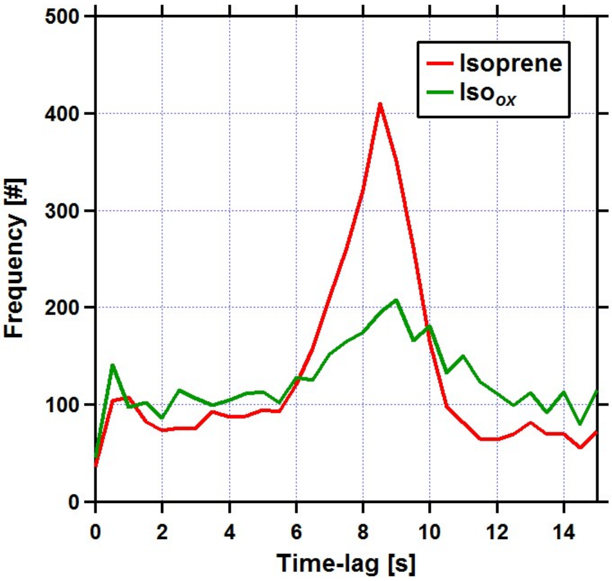

Figure S1. Histogram of time-lag measurements for isoprene and the sum of its oxidation products, Iso_{ox} (MVK+MACR+ISOPOOH). The histogram peaks at 8.5 s for isoprene and 9 s for MVK+MACR which were used as the prescribed time-lag for each compound in the data processing.

1.4 Measurements of Black Carbon

A Multi Angle Absorption Photometer (MAAP, Thermo Inc., Model 5012)(19) provided black carbon (BC) concentrations at a one minute time resolution. These data were subsequently averaged to the same 45 minute time resolution as the flux measurements. The instrument measures aerosol light absorption at 637 nm, and BC concentration is estimated assuming a mass absorption coefficient of 6.6 m^2g^{-1}. A 5% correction was applied to the data to account for an adjustment of wavelength(20). Aerosol was sampled from 38.8m above ground level using a PM_{10} inlet, relative humidity of the sampled air was kept between 20% and 50% using an automated dryer(21) .

Additional measurements of BC[(22)] and nitric oxide[(23)] were obtained from the T3 measurement site used in the GoAmazon campaign. The data collected covered the period February 2014 to June 2015. Figure S2 shows a comparison of NO concentrations with BC. There is a clear relationship between the two species which demonstrates that BC, on a time scale of days to months, can give an accurate reflection of temporal patterns of NO concentration. However, from this relationship it is not feasible to infer the NO concentrations at the ZF2 site. This is because the slope and intercept are likely to vary at different locations in Amazonia. The slope reflecting the different atmospheric lifetimes of BC and NO and thus distance from emission source and intercept reflecting the background NO concentrations which are driven by soil emissions.

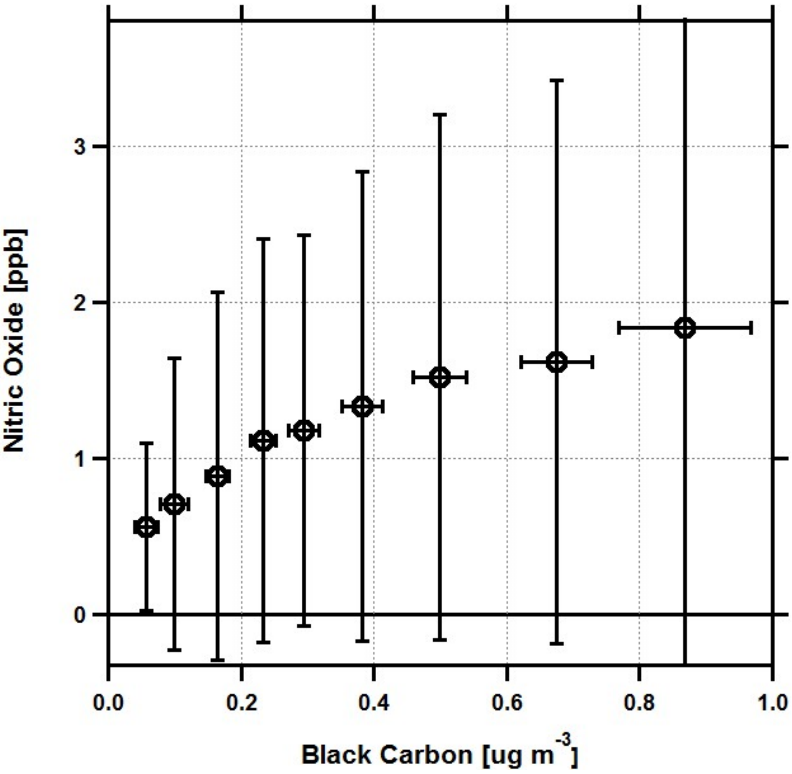

Figure S2. Scatter plot showing the measured relationship between nitric oxide (NO) and black carbon (BC) at the T3 measurement site, Manacapuru, Brazil. The data were stratified such that each data point represents the median of 1228 hourly measurements. Error bars represent ±1 σ.

2. Isoprene Emission Potentials

Isoprene emission potentials were calculated on a monthly basis by adopting the approach of Langford et al. (2017)[(24)]. This method involves normalising the measured fluxes to a set of standard conditions to yield the emission potential (also termed the base emission rate). Here, we use the Model of Emission of Gases and Aerosols from Nature (MEGAN 2.1(25, 26)) in conjunction with a canopy environment model with the standard conditions as described by Langford et al. (2017)(24). The model requires information on the photosynthetic photon flux density (PPFD) and temperature as well as optional parameters including leaf area index, CO_2 concentration and soil moisture. There was insufficient coverage in CO_2 and soil moisture data over the 11-month period, so CO_2 was kept constant at 400 ppm and the soil moisture algorithm not applied. PPFD fluxes were measured by the National Institute for Amazonian Research (Instituto Nacional de Pesquisas da Amazônia, INPA) at the nearby K34 tower, located 1.6 km south of TT34. Given the typical flux footprint area of (~1 km), photosynthetically active radiation (PAR) values from K34 are considered to be representative of both sites. PAR was measured above the canopy at 51.6 m using a LI-190, SZ Li-COR sensor. Measurements were converted to PPFD at 400 nm and 700 nm and the mean taken. Ambient temperature measurements were taken from the Gill R3 sonic anemometer situated at TT34. The temperature measured by sonic anemometers can be subject to offsets and also errors due to the humidity of the ambient air. Therefore, temperature data from the anemometer were corrected by comparison against a weather station (DAVIS Vantage Pro 2) situated at 42 m on the TT34 tower and verified against temperatures measured at K34 at 51.1 m with a Pt resistance (PT100) and Vaisala HMP45AC temperature and relative humidity probe (INPA).

Leaf area index (LAI) measurements determined from the MODIS satellite were used to provide MEGAN with an appropriate seasonal cycle of leaf phenology over a 13-year period between 2002 and 2013. Here the global MCD15A2 MODIS Combined Terra and Aqua LAI and FPAR product [Myneni et al, 2015] which comprises 8-day composites at 1 km resolution was used, with the data re-projected (from their native sinusoidal grid) and then re-gridded to a 0.25 x 0.25 generic grid, using only cloud free observations of the best quality (determined using the product's quality flags). The 8-day composites were then assembled into monthly mean values, weighting each specific composite accordingly by the amount it overlapped a given month. Figure S3 shows the 2002-2013 mean LAI seasonal variation at the ZF2 site; the error bars show the ±1 standard deviation of the mean values. Figure S3 shows that the LAI at the site is typically lowest in March and April (LAI = 4 m^2/m^2) and largest during the dry season, peaking at 6 m^2/m^2 in the month of September.

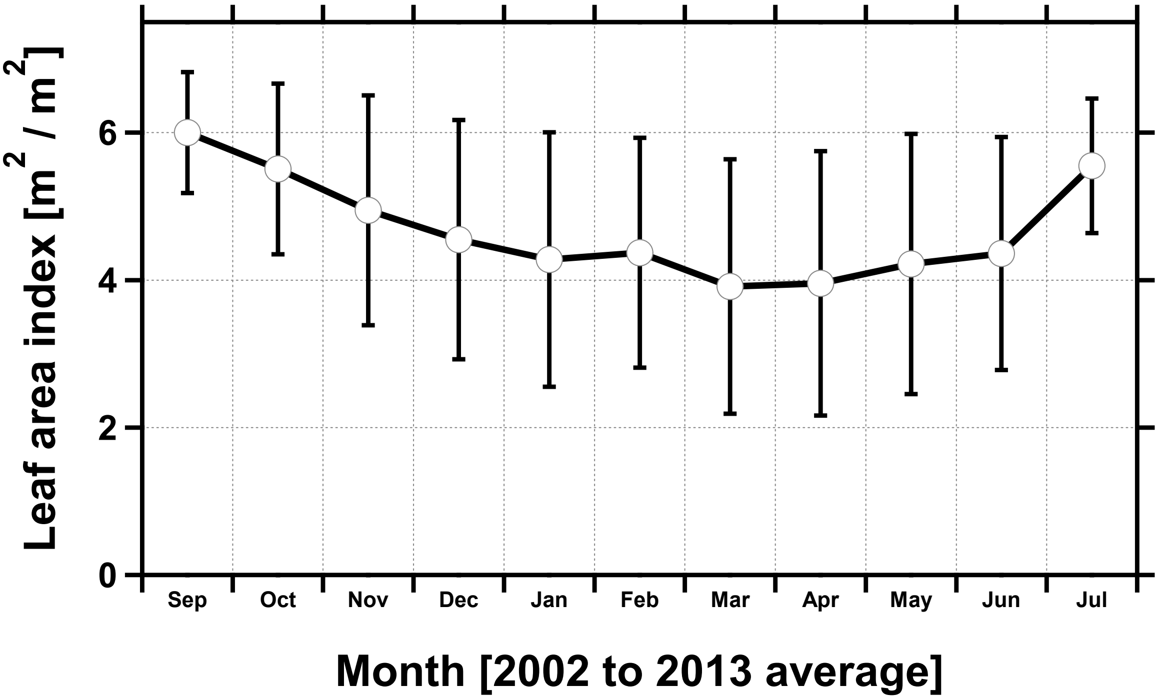

Figure S3. Monthly Leaf Area Index inferred from the Modis Satellite observations between 2002 and 2013.

Within the MEGAN algorithm, the isoprene flux, F_{iso}, is calculated as

$$F_{iso} = IEP \times \gamma \quad , \qquad (1)$$

where *IEP* is the isoprene emission potential for a set of standard conditions (303 K and 1500 PPFD) and γ is a scaling factor. The γ term is the sum of the light (γ_L) and temperature response curve (γ_T) which describe how isoprene emission rates from vegetation change with environmental conditions. Each response curve is normalised to unity at standard conditions and therefore γ is dimensionless. Running the algorithm with the *IEP* set to one allows the calculation of the scaling factor, γ, required to normalise ambient light and temperature to standard conditions on a point-by-point basis. The isoprene emission potential for each month of the study was subsequently calculated following the recommendations of Langford et al. (2017)$^{(24)}$ where the monthly average isoprene flux ($\bar{F}_{iso}$) is divided by the monthly average scaling factor ($\bar{\gamma}$):

$$IEP_{weighted} = \frac{\bar{F}_{iso}}{\bar{\gamma}} \ . \qquad (2)$$

In our analysis we only used the flux measurements during daytime, between the hours of 09:00 and 17:00 (consistent with Figure 1 in the main manuscript), when fluxes were largest. Using this weighted approach ensures that the use of the calculated emission potential will always yield fluxes with the same average as the observations (24). The median isoprene emission potential for the 11 month period was 6.9 mg m^{-2} h^{-1}. This compares remarkably closely with the default value of 7 mg m^{-2} h^{-1} used in MEGAN for deciduous tropical forests.

3. Resistance Analysis

The deposition process is driven by turbulence and as such, the data we included for the resistance analysis were first filtered according to the measured friction velocity parameter, u_*, removing data below a threshold of 0.3 m s^{-1}. This threshold represented the best compromise between removing those data associated with low turbulence and hence greater uncertainties, with the need to maintain sufficient data for a robust analysis. Massman and Lee (2002)(27) reviewed the eddy covariance literature and found that typical u_* thresholds ranged between 0 and 0.6 m s^{-1} which places our chosen threshold in the centre of typical values used. The u_* filter also eliminates from our analysis data during which the transport resistances become very large. In those conditions canopy resistances would need to be derived, with more uncertainty, as the difference between two large resistances.

The analysis of resistances at our site shows that the theoretical maximum deposition velocity ($V_{\mathrm{dmax}} = R_a+R_b$) is near constant throughout the year (~35 s m^{-1}) which confirms that the seasonal cycle in $\mathrm{Iso_{ox}}$ deposition velocity is not a consequence of changes in meteorology. In contrast, the canopy resistance of total $\mathrm{Iso_{ox}}$ changes by up to a factor of nine between the wet and dry seasons. One possible explanation is that R_c changes due to seasonal variations in canopy properties, the most important being canopy wetness. We discount this hypothesis for a combination of two factors: on the one extreme, Nguyan et al. (2015)(28) show that the canopy resistance of ISOPOOH is close to zero independent of surface wetness, and thus the deposition is limited by turbulence and not canopy wetness. On the other end of the spectrum, the effective Henry's law constants for MVK and MACR are very small (41 and 6.5 M atm^{-1} respectively(29)) such that solubility effects are considered negligible for both of these compounds in typical model parameterizations(30, 31). A second possibility is that MVK+MACR is emitted directly from the vegetation due to within leaf oxidation of isoprene during the warmer months of the dry season or via conversion of ISOPOOH to MVK upon contact with the leaf surface(32). However, within leaf oxidation occurs only under extreme heat stress and would not be expected to be significant within the temperature range experienced during our measurement period. This is further supported by the work of Jardine et al. (2012)(33) who found isoprene oxidation in the atmosphere to dominate isoprene oxidation within plants at the ZF2 site during the dry season. In addition, any ISOPOOH converted to MVK has been shown to convert to Methyl ethyl ketone before re-emission from the leaf(32).

The remaining explanation is that the seasonal change in $\mathrm{Iso_{ox}}$ deposition velocities is in fact driven by changes in the relative abundances of the three species that are detected at *m/z* 71 in the PTR-MS (e.g. $\mathrm{Iso_{ox}}$). This is because these compounds have very different physio-chemical properties, for example, as discussed above, ISOPOOH has a lower vapour pressure, greater solubility and ultimately much lower canopy resistance and therefore should deposit significantly faster than MVK+MACR. Indeed, field observations above temperate forests in the U.S. appear to confirm this to be the case with measurements of ISOPOOH+IEPOX having a zero canopy resistance(28). In previous work, Liu et al. (2016)(34) took advantage of these differences to calculate the fraction of ISOPOOH observed at *m/z* 71 in their PTR-time-of-flight instrument. Sampling sequentially between ambient air and air sampled through a cold trap allowed the contribution of ISOPOOH to be separated by difference. This is because ISOPOOH has a vapour pressure some three orders of magnitude lower than MVK+MACR, meaning it was efficiently removed by the cold trap. In our flux measurement setup it was not possible to switch between two such inlets, we therefore, utilise the fact that MVK+MACR and ISOPOOH have very different deposition velocities and calculate the fraction of ISOPOOH (f_{ISOPOOH}) detected at *m/z* 71 as following Eq. 1 of the main manuscript.

4. Calculation of ISOPOOH to MVK+MACR production ratios

Table S2 shows the loss rates used in the production ratio calculation with respect to reaction with OH (ki_{OH}), entrainment (ki_{en}) and deposition to the surface (ki_{dep}) for each of the four species ((1,2)- and (4,3)- ISOPOOH, MVK and MACR).

Table S2. The loss rates for (1,2)- and (4,3)- ISOPOOH, MVK and MACR with respect to OH, dry deposition and entrainment. Here, the first order rate coefficient $k_i = (k_{i\,OH} + k_{i\,dep} + k_{i\,en})$ with units of s^{-1}

$k_{i\,\mathrm{OH}}$	$k_{i\,\mathrm{OH}}$	$k_{i\,\mathrm{OH}}$	$k_{i\,\mathrm{OH}}$	k_{dep}	k_{dep}	k_{en}	k_i	k_i	k_i	k_i
(1,2)- ISOPOOH	(4,3)- ISOPOOH	MVK	MACR	ISOPOOH	MVK + MACR	All	(1,2)- ISOPOOH	(4,3)- ISOPOOH	MVK	MACR
3.70E-05	5.90E-05	1.00E-05	1.40E-05	4.5E-05	4.5E-06	1.0E-05	9.20E-05	1.14E-04	2.25E-05	2.65E-05

4.1 Calculation of Oxidation Pathways

Having established the production ratios of ISOPOOH to MVK+MACR on a monthly basis, we combined our findings with detailed chemical box model simulations incorporating the Master Chemical Mechanism (MCM), described below, to estimate (i) the level of NO at our site and (ii) the fractional contribution of the four major oxidation pathways for ISOPOO reactive loss. Figure S4, panel (a), shows the relationship between the ISOPOOH to MVK+MACR production ratio for a given NO concentration as predicted by the MCM box model for the average daytime isoprene concentration (5.8 ppb) found in the month of September. Panel (b) shows the fractional contribution of the four reaction pathways, f_{HO2}, f_{NO}, f_{RO2} and f_{ISOM} over the same range of NO concentrations. Using an equivalent of these two plots for each month as a lookup table, we were able to estimate the fraction of ISOPOO that reacts via each pathway, as shown in Figure 4 of the main manuscript, based on our observed production ratios. This approach yielded estimated NO concentrations at our site that ranged between 41 ppt (March) and 139 ppt (October). Previous studies have reported background concentrations of NO above the Amazon in the range of 15 to 80 ppt(34-36), which places our estimates in the midrange of observations, lending further confidence to our approach.

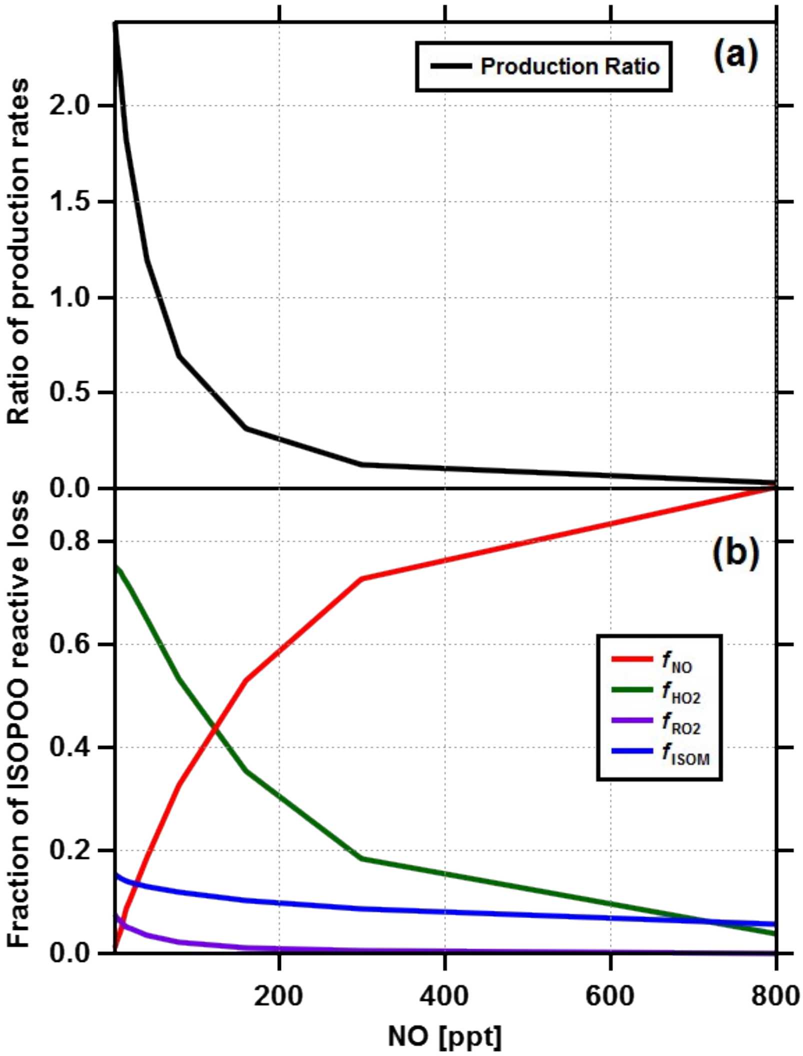

Figure S4. The output from the Master Chemical Mechanism box modelling study which calculates the ratio of ISOPOOH to MVK+MACR production rates over a given range of NO concentrations (a) and the corresponding reactive loss to be expected to each of the four degradation pathways f_{NO}, f_{HO2}, f_{RO2} and f_{ISOM} (b) for the average conditions of the month of September ([isoprene] = 5.8 ppb).

Figure S5 shows the relative contribution of each oxidation pathway on a monthly basis for a scenario where we assume no anthropogenic influence throughout the year and maintain the NO concentrations at 35 ppt, which is the value established for background conditions in Amazonia by the GoAmazon aircraft campaign(34). These may differ from average column values owing to an increase in concentrations towards the surface, but they give the most recent picture of background conditions in Amazonia. This plot shows that even when NO is held constant there is some variability in the relative contributions of the four major oxidation pathways that appears to relate to the concentration of isoprene used in the box model. This variation, is however, small compared to the changes imposed by increasing NO at the low end of the scale.

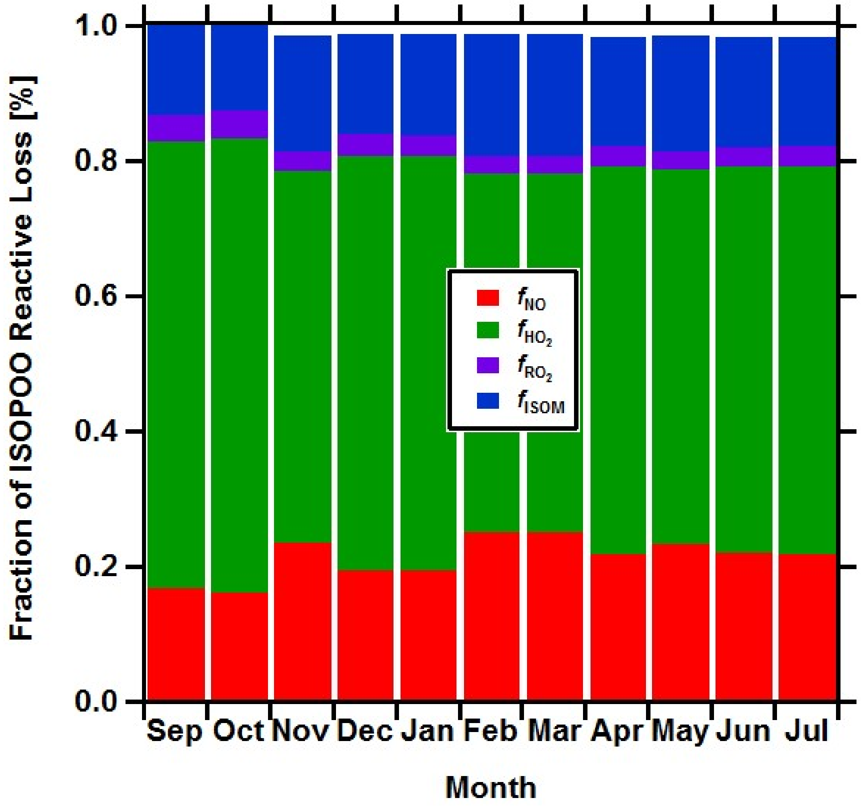

Figure S5. The fraction of ISOPOO reactive loss that is predicted by the MCM box model when the NO concentrations are held at 35 ppt throughout the year to represent a situation where there is no anthropogenic influence on isoprene oxidation chemistry.

5. Modelling approach

5.1 Box modelling

The box model was initialised with concentrations of [OH] fixed at 5×10^5 cm^{-3} (as measured for 'background' conditions in Amazonia during the GoAmazon experiment(34, 37), [O_3] at 10 ppbv, [CH_4] of 1.85 ppmv and [CO] of 110 ppbv, and T = 298 K. Entrainment loss rates for all model species were set to 1×10^{-5} cm^{-3} s^{-1} (34, 38). For the box model, a column average value of V_d was calculated according to the functionalities of each species. These values are based on the reported rates in Nguyen et al.

(2015)$^{(28)}$ and are given in Table S3. A boundary layer height (*BLH*) of 1.5 km was assumed, in the range observed by Nguyen et al. (2015)$^{(28)}$. Loss rates for each species to dry deposition are then $L_d = V_d/BLH$. Photolysis rates were fixed to mean rates for the day time period 09:00-17:00 calculated for July 1. The model was then run to steady state for a range of fixed [NO] from 0 - 800 pptv.

The monthly model output values for IEPOX production and steady state HCHO mixing ratio reported in the main manuscript (Figure 4) are constrained with the measured mean daytime (09:00 - 17:00) isoprene mixing ratios for each month (Figure 1; averages range from 3.1 ppbv in July, to 7.1 ppbv in October). OH is assumed to be constant for the model runs. However, recent work has shown that OH concentrations in the Amazon increase with increasing NO$^{(37)}$. This is in contrast to a previous meta-study $^{(39)}$, which suggested that at the low NO concentrations typical of the Amazon, OH concentrations were insensitive to changes in [NO_x]. Taking the work of Liu et al. (2018)$^{(37)}$, then [HCHO] might be expected to be even more sensitive to increasing NO than shown here for fixed OH, as increasing NO will both increase f_{NO} (Figure S6) and the rate of isoprene oxidation.

Figures S6-S7 show model output from an example run with [C_5H_8] fixed at 5.0 ppbv, which is within the observed range of daily mean values (Figure 1).

Table S3. Dry deposition velocities applied to all species based on their functional groups – based on Nguyen et al. (2015)(28)

Functional group / species	Dry deposition velocity ($V_{d(s)}$ (cm s^{-1})
Hydroperoxide	4.5
H_2O_2	5.2
Organic nitrate	2.0
HNO_3	3.8
Organic acid	1.0
Oxygenated VOC	0.45
Other	0.1

5.2 Box modelling results

ISOPOO is defined here as the sum of the seven initial peroxy radicals ($ISOPAO_2$, $ISOPBO_2$, $ISOPCO_2$, $ISOPDO_2$, $CISOPAO_2$, $CISOPCO_2$, $ISOPO_2$) that can be formed from the reaction of the OH-isoprene adducts, formed from the addition of OH to isoprene, with O_2 (40). Each ISOPOO peroxy radical can react with NO, HO_2, RO_2, or can isomerise – either to stable products or to form secondary peroxy radical species. At [NO] > 500 pptv, reaction with NO is the dominant loss process, accounting for *ca.* 90% of the ISOPOO reactions, with the remaining losses through isomerization. The NO channel produces the stable carbonyl products, HCHO, MVK and MACR in high yield(40). At lower [NO], typical of conditions observed in the Amazon(34), the HO_2 channel and isomerization (for $CISOPAO_2$ and $CISOPCO_2$) become increasingly important. The reaction of ISOPOO with HO_2 leads to hydroperoxides that can subsequently react with OH to give IEPOX(41).

Figure S4, shows the amount of ISOPOO going through each channel for a fixed $[C_5H_8] = 5.8$ ppbv (the daytime mean for the month of September), and $[OH] = 5 \times 10^5$ cm^{-3} as a function of [NO]. The contributions of the NO (f_{NO}) and HO_2 (f_{HO2}) channels are equal at roughly 110 ppt of NO. Below 100 ppt of NO, the isomerization channel (f_{ISO}) accounts for 15 – 18 % of the loss of ISOPOO.

Figure S6 shows the HO_2 and RO_2 concentrations simulated in the model for the model run with $[C_5H_8] = 5.0$ ppb and $[OH] = 5 \times 10^5$ cm^{-3} as a function of [NO]. At very low [NO] (< 20 ppt), $[RO_2] > [HO_2]$, although HO_2 dominates the reaction of ISOPOO because $k(ISOPOO + HO_2) >> k(ISOPOO + RO_2)$(40). As [NO] increases, $[RO_2]$ falls rapidly, with $[HO_2]$ falling less rapidly and becoming greater than RO_2.

Figure S7 shows the steady state HCHO mixing ratio (ppb) and IEPOX production rate (ppt min^{-1}) for the model run with [C_5H_8] = 5.0 ppb and [OH] = 5 × 10^5 cm^{-3} as a function of [NO]. The simulated steady state HCHO mixing ratio increases rapidly from 8 ppb at an NO concentration of 40 ppt to about 9ppb at NO concentrations of 150 ppt, which represents the range of NO concentrations implied by our observations and box modelling. The production rate of IEPOX (produced from ISOPOOH + OH), decreases rapidly with increasing [NO] because there is less ISOPOOH produced through the RO_2 + HO_2 channel.

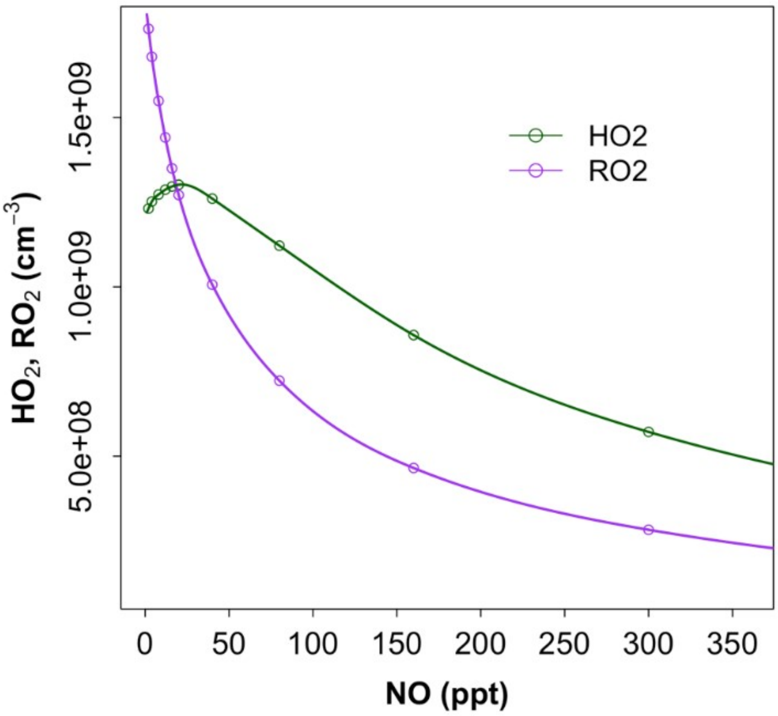

Figure S6. Model simulated concentrations of HO_2 and RO_2 for a model run using a fixed [C_5H_8] of 5.0 ppb and fixed [OH] of 5 × 10^5 cm^{-3}, as a function of [NO].

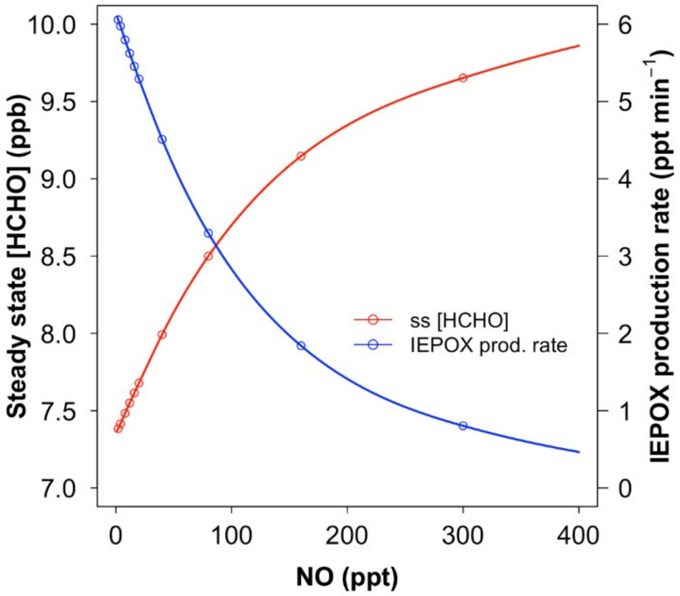

Figure S7. Model simulated mixing ratio of HCHO at steady state (ss [HCHO]) and the IEPOX production rate for a model run using a fixed [C_5H_8] of 5.0 ppb and fixed [OH] of 5 x 10^5 cm^{-3}, as a function of [NO].

5.3 Simulations of Oxidation Chemistry using a Chemical Transport Model

We use the global GEOS-Chem chemical transport model (v10-01; http://wiki.seas.harvard.edu/geos-chem/index.php/GEOS-Chem_v10-01) to determine consistency of current models with observed seasonality in isoprene oxidation chemistry. The model is at 2° × 2.5° (latitude × longitude) horizontal resolution and is sampled hourly coincident with the ZF2 following 2 months spin-up for chemical initialization. The model is driven with GEOS-FP assimilated meteorology from the NASA Global Modelling and Assimilation Office (GMAO). Biogenic emissions of isoprene are from the Model of Emissions of Gases and Aerosols (MEGAN 2.1)(26). Sources of NO_x included in the model and relevant to South America are from Hudman et al.(42) for soils, GFED version 4(43) for seasonal open fires, and EDGAR v4.2 for anthropogenic activity and biofuel use.

Isoprene secondary organic aerosol (SOA) formation in GEOS-Chem is via irreversible reactive uptake to aqueous aerosol as described in Marais et al.(44) and is coupled to detailed gas-phase isoprene chemistry(45) and depends strongly on sulphate abundance(46). All other SOA from monoterpenes, sesquiterpenes and aromatics is formed via reversible partitioning to dry organic aerosol as described in Pye et al.(47).

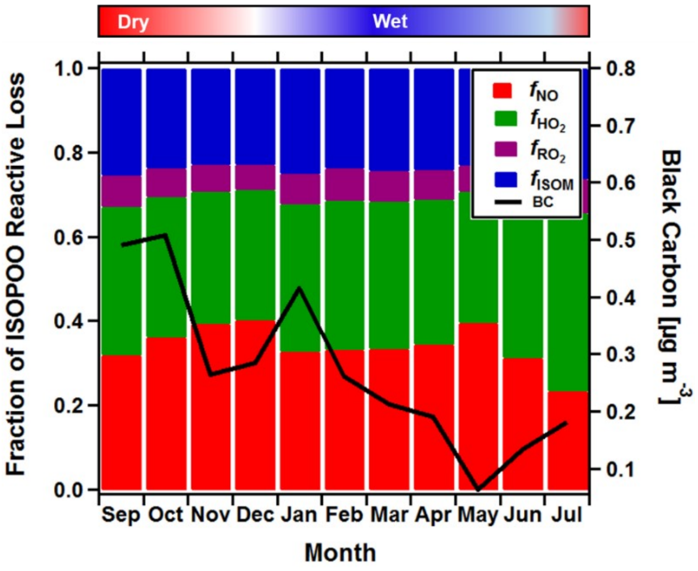

Figure S8. The fraction of ISOPOO reactive loss to the four major oxidation pathways, f_{NO}, f_{HO2}, f_{RO2} and f_{ISOM} as predicted by the GEOS-Chem model over central Amazonia on a monthly basis between September 2013 and July 2014. The black line shows the black carbon concentration measured at the ZF2 site.

Figure S8 shows the fractional contribution of the four major oxidation pathways predicted by the model on a monthly basis for 2013 to 2014 from the grid cell coincident with the ZF2 measurement site. While there is some seasonal variation in the NO pathway, with higher values in November and December and lower contributions in June and July, the model is unable to capture the dynamic range we predict using our observations and MCM model runs. The model slightly over-predicts the contribution of the NO pathway in the wet season and under predicts its contribution in the dry season.

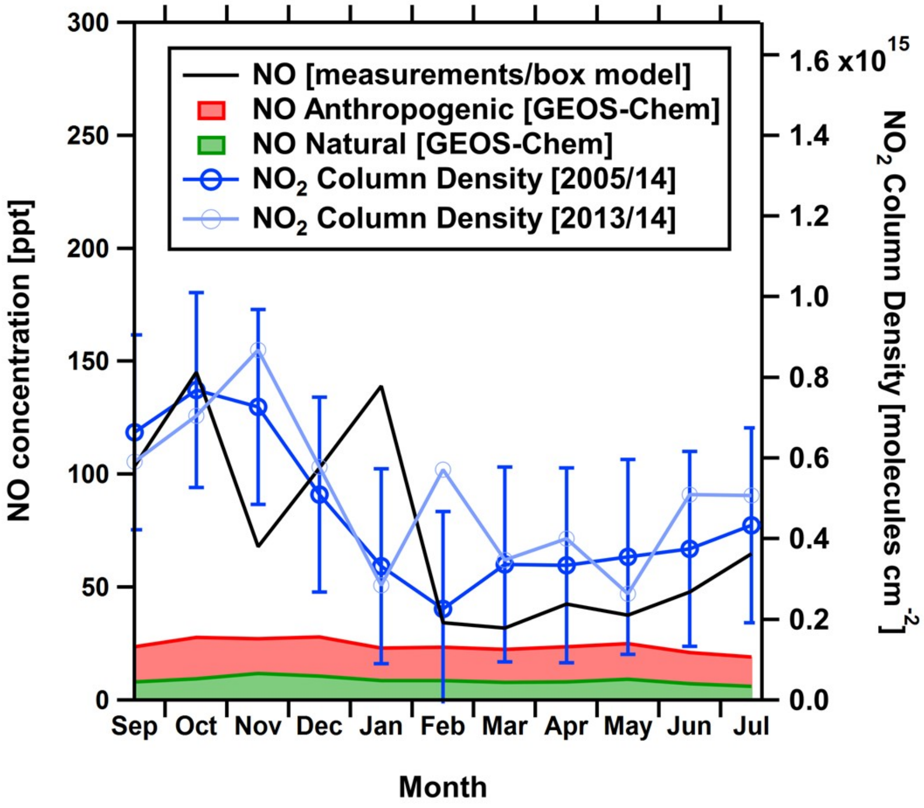

Figure S9 Comparison of the NO concentration predicted through the combination of field measurements and box MCM model with those predicted by the GEOS-Chem chemical transport model. The NO predicted by GEOS-Chem is further divided into that originating from anthropogenic and natural (soil) sources between September and July, 2013/14. Average column densities of NO2 from satellite are shown for the period of 2005 to 2014 together with column densities coinciding with the measurement period.

Figure S9 shows a comparison of the NO concentrations predicted by the GEOS-Chem model with the NO concentrations implied from those derived using our measurements of isoprene chemistry and box modelling. This plot reveals that GEOS-Chem predicts approximately 30% lower NO concentrations during the wet season and four times lower in the dry season. Local anthropogenic and biomass burning emissions account for over half the total NO concentrations in GEOS-Chem (determined by switching off all anthropogenic and biomass burning emissions), but there is very little temporal variation and no distinct seasonality in NO. In the GEOS-Chem model run, [NO] is of the order of 28 pptv for the whole year, similar to the mixing ratio that is used in the box model run shown in Figure S5. However, the GEOS-Chem model run predicts a significantly higher ratio for $f_{\mathrm{NO}}/f_{\mathrm{HO2}}$ (roughly unity) than the box model run (~0.33). This demonstrates the sensitivity of the fate of ISOPOO to isoprene and OH concentrations (see Figure S10 below and e.g. Newland et al., 2020(48)). Higher C_5H_8 and/or OH will lead to higher modelled HO_2 concentrations and hence a lower f_{NO}/f_{HO2} ratio, shifting the cross-over point (where $f_{NO} = f_{HO2}$) to a higher [NO].

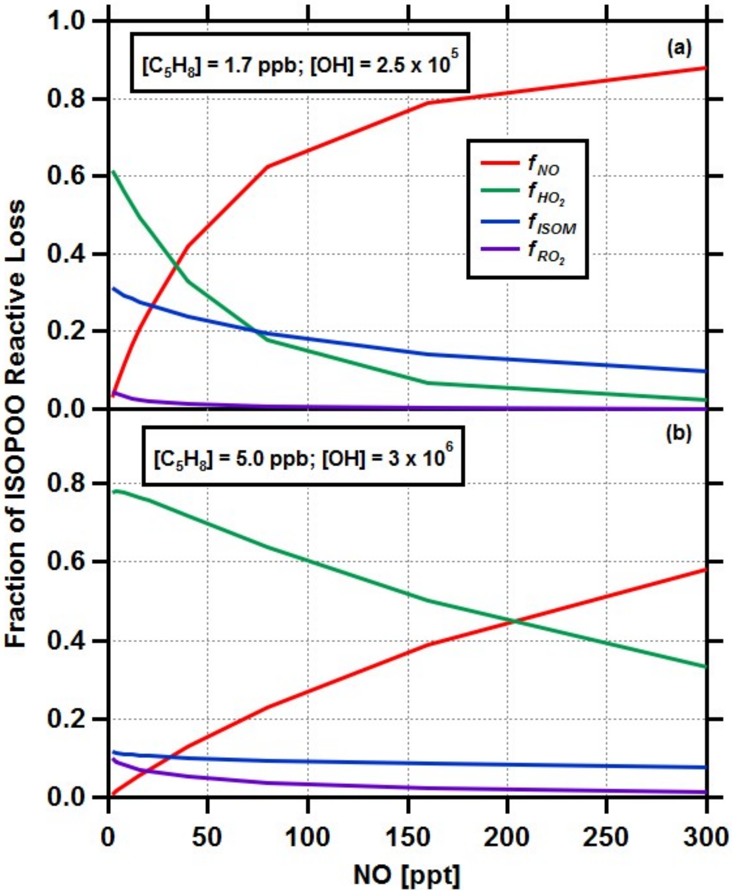

Figure S10. The effect of C_5H_8 and OH concentrations on the f_{NO}/f_{HO2} ratio determined in the box model.

6. Sensitivity Studies

6.1 Impact of changing hydroxyl concentration

Liu et al. (2016)(34) use a daytime value of [OH] of 5.0×10^5 cm^{-3} which is based on average daytime observed OH concentrations at their measurement site under "clean" conditions. For consistency we also adopt this value in the detailed MCM box modelling although, as mentioned in Section 5.1, it is possible that the concentration of OH undergoes some seasonal trend. For example, Liu et al. (2018)(37) suggest that OH might increase during periods when NO is elevated, and more recent work by Shrivastava et al. (2019)(49) shows high concentrations of NO_x (>0.2 ppb) in the Manaus plume to dramatically increase the oxidising capacity and subsequently the formation of aerosols. Furthermore, Barkley et al. (2009)(50) postulated whether a drop in OH concentration during the transitional period between dry and wet seasons, when NO concentrations are at their lowest, might account for the marked dip in formaldehyde concentrations at this time of year.

One approach for assessing the seasonal variation in OH is to look at the ratio of directly observed isoprene fluxes to concentrations, which, assuming OH is the primary sink for isoprene, should remain constant if no seasonal pattern is present. In fact, the ratio is larger during the dry season and lower in the wet season which is consistent with the hypothesis of Barkley et al. (2009)(50). Yet, this observation should be treated with some caution as this ratio may additionally reflect a difference is boundary layer height between dry and wet seasons, which would act to lower concentrations as the BLH increases in the dry season. For this reason, we kept the OH concentration used in the MCM modelling constant at 5.0×10^{5} cm^{-3}, but here we perform a sensitivity study to see how our results might have changed had we adopted an OH concentration that varied by month.

Table S4 The loss rates for (1,2)- and (4,3)- ISOPOOH, MVK and MACR with respect to OH, dry deposition and entrainment on a monthly basis assuming a seasonal cycle in OH concentrations. Here, the first order rate coefficient $k_i = (k_{i\,OH} + k_{i\,dep} + k_{i\,en})$ with units of s^{-1}

Month	*OH* *(cm^{-3})*	$k_{i\,\mathrm{OH}}$	$k_{i\,\mathrm{OH}}$	$k_{i\,\mathrm{OH}}$	$k_{i\,\mathrm{OH}}$	k_{dep}	k_{dep}	k_{en}	k_{i}	k_{i}	k_{i}	k_{i}
		(1,2)-ISOPOOH	(4,3)-ISOPOOH	MVK	MACR	ISOPOOH	MVK + MACR	All	(1,2)-ISOPOOH	(4,3)-ISOPOOH	MVK	MACR
Sep	9.22E+05	6.8E-05	1.1E-04	1.8E-05	2.6E-05	4.5E-05	4.5E-06	1.0E-05	1.2E-04	1.6E-04	3.3E-05	4.0E-05
Oct	8.35E+05	6.2E-05	9.8E-05	1.7E-05	2.3E-05	4.5E-05	4.5E-06	1.0E-05	1.2E-04	1.5E-04	3.1E-05	3.8E-05
Nov	4.95E+05	3.7E-05	5.8E-05	9.9E-06	1.4E-05	4.5E-05	4.5E-06	1.0E-05	9.2E-05	1.1E-04	2.4E-05	2.8E-05
Dec	5.89E+05	4.4E-05	7.0E-05	1.2E-05	1.6E-05	4.5E-05	4.5E-06	1.0E-05	9.9E-05	1.2E-04	2.6E-05	3.1E-05
Jan	5.96E+05	4.4E-05	7.0E-05	1.2E-05	1.7E-05	4.5E-05	4.5E-06	1.0E-05	9.9E-05	1.3E-04	2.6E-05	3.1E-05
Feb	5.51E+05	4.1E-05	6.5E-05	1.1E-05	1.5E-05	4.5E-05	4.5E-06	1.0E-05	9.6E-05	1.2E-04	2.6E-05	3.0E-05
Mar	5.00E+05	3.7E-05	5.9E-05	1.0E-05	1.4E-05	4.5E-05	4.5E-06	1.0E-05	9.2E-05	1.1E-04	2.5E-05	2.9E-05
Apr	5.67E+05	4.2E-05	6.7E-05	1.1E-05	1.6E-05	4.5E-05	4.5E-06	1.0E-05	9.7E-05	1.2E-04	2.6E-05	3.0E-05
May	6.36E+05	4.7E-05	7.5E-05	1.3E-05	1.8E-05	4.5E-05	4.5E-06	1.0E-05	1.0E-04	1.3E-04	2.7E-05	3.2E-05
Jun	7.82E+05	5.8E-05	9.2E-05	1.6E-05	2.2E-05	4.5E-05	4.5E-06	1.0E-05	1.1E-04	1.5E-04	3.0E-05	3.6E-05
Jul	8.77E+05	6.5E-05	1.0E-04	1.8E-05	2.5E-05	4.5E-05	4.5E-06	1.0E-05	1.2E-04	1.6E-04	3.2E-05	3.9E-05

For this exercise, the seasonal pattern in OH was determined from the ratio of isoprene fluxes to concentrations and then converted to a concentration by normalising the ratio to 5.0×10^{5} cm^{-3} for the month of March, when Liu et al. (2016)(34) made their OH observations. Table S4 shows how the loss rate terms for ISOPOOH, MVK and MACR change on a monthly basis due to the changing OH concentration. Figure S11 directly compares the calculated production rates of ISOPOOH to MVK+MACR under static and dynamic OH concentrations. The results show that the OH concentration has a relatively minor effect on the ISOPOOH to MVK+MACR production rates, with the largest increases of up to 15 % in September.

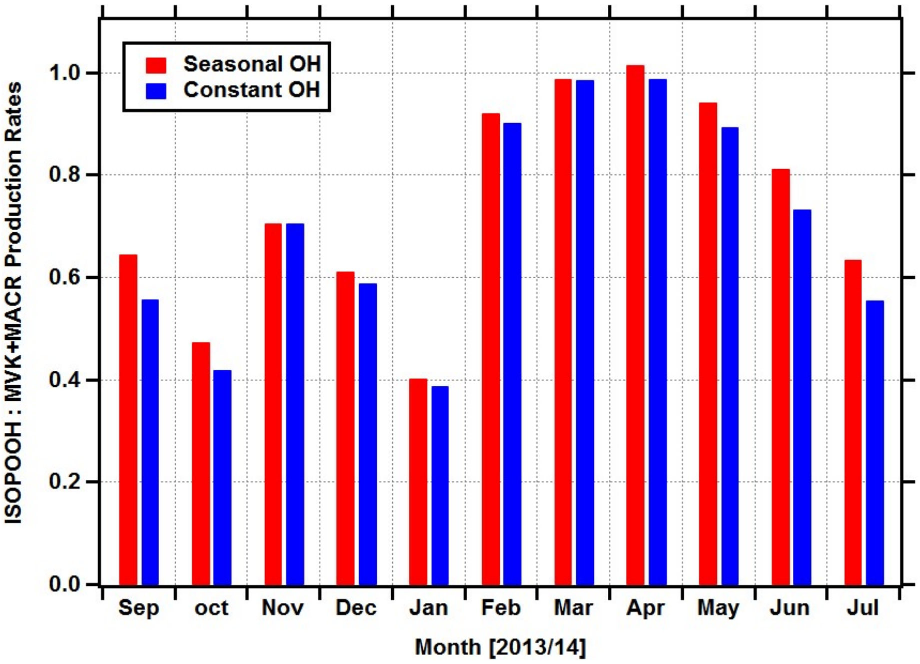

Figure S11. Calculated ISOPOOH to MVK+MACR production ratios assuming that OH is constant throughout the year at 5 ×10^5 molecules cm^{-3} (Blue) and assuming a seasonal cycle in OH (red), as is implied by the ratio of isoprene fluxes to concentrations.

Figure S12 shows the how the fraction of ISOPOO reactive loss would change if we assumed the seasonal cycle in OH described above.

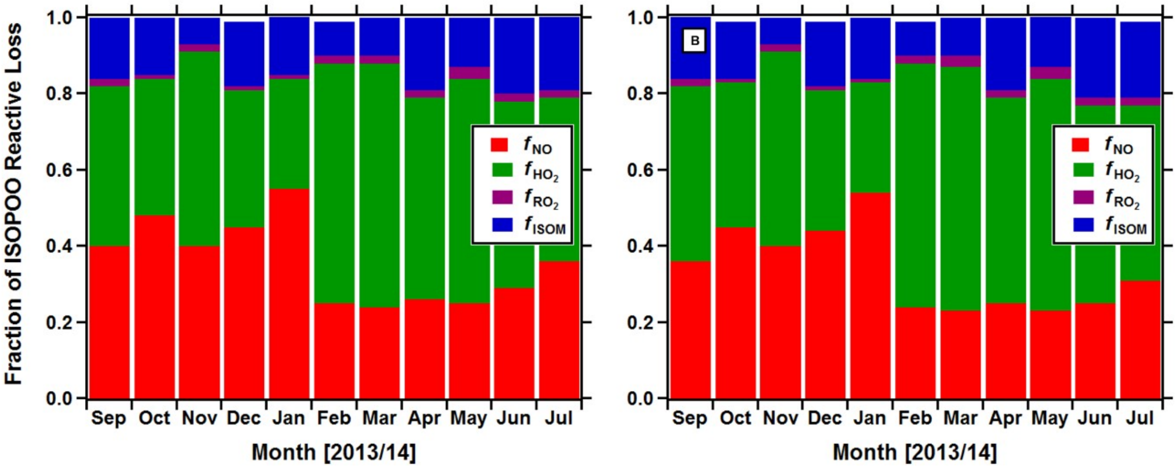

Figure S12 Panel A shows the fraction of ISOPOO reactive loss via the NO, HO$_2$, RO$_2$ and isomerisation pathways when OH concentrations are held at 5 x 10^5 molecules cm-3 and Panel B,

where OH concentrations vary dynamically to reflect the OH sink strength implied by the ratio of isoprene fluxes to concentrations.

6.2 Calculation of the ISOPOOH contribution to *m/z* 71

Our deposition velocity approach to determining the relative fraction of ISOPOOH makes the assumption that ISOPOOH is efficiently detected at *m/z* 71 over the whole year. On entering the PTR-MS the (1,2)- and (4,3)-ISOPOOH molecules fragments upon contact with hot metal surfaces in the instrument (e.g. the heated silco-steel inlet and drift tube), losing a peroxy radical to form MVK and MACR, respectively(11). Liu et al. (2016)(34) used synthesized ISOPOOH standards to demonstrate that in their PTR-TOF-MS instrument conversion efficiency was around 95%. We maintained our drift tube and inlet temperatures at 50 °C, some 30 °C lower than that used by Liu et al. (2016)(34), but our older PTR-MS instrument (manufactured in 2004) contained a heated silco-steel capillary inlet, rather than the more commonly used PEEK capillary and thus provided additional metal surfaces for conversion to take place. Critically, the PTR-MS operating conditions, including the drift tube and inlet temperature were kept constant throughout the 11-month measurement period.

A second assumption of our approach is that the surface deposition velocities we assign to ISOPOOH (4.5 cm s^{-1}) and MVK+MACR (0.45 cm s^{-1}) are realistic. We can draw confidence in the value used for ISOPOOH because, as already discussed in Section 3, previous measurements by Nguyen et al. (2015)(28) report ISOPOOH+IEPOX to deposit with a zero canopy resistance and when extracting their measurements to the surface (e.g. $1/R_b$) we obtain a deposition rate of 4.3 cm s^{-1}. At the ZF2 site the average maximum deposition velocity (e.g. $1/(R_a+R_b)$) was 2.9 cm s^{-1}, which when extrapolated to the surface (e.g. $1/R_b$) was 4.5 cm s^{-1} and very similar to that reported by Nguyen et al. (2015) for measurements of ISOPOOH+IEPOX. As we use an Rc of zero, we cannot increase the deposition velocity any further, but we can explore the implications of a non-zero canopy resistance by reducing the $V_{d(s)}$ to 3.5 cm s^{-1}. Determining the deposition velocity for MVK+MACR is more challenging due to a lack of MVK+MACR specific measurements, but we can perform a sensitivity study on our results by varying the MVK+MACR deposition velocity to the range of values presented by Zhang et al. (2003)(30).

Figure S13 shows how the production ratio of ISOPOOH to MVK+MACR changes as the deposition velocities assigned to MVK+MACR and ISOPOOH are adjusted within these set constraints. Based on this analysis, the uncertainty associated with our calculated production ratios is on the order of plus 21% and minus 7%.

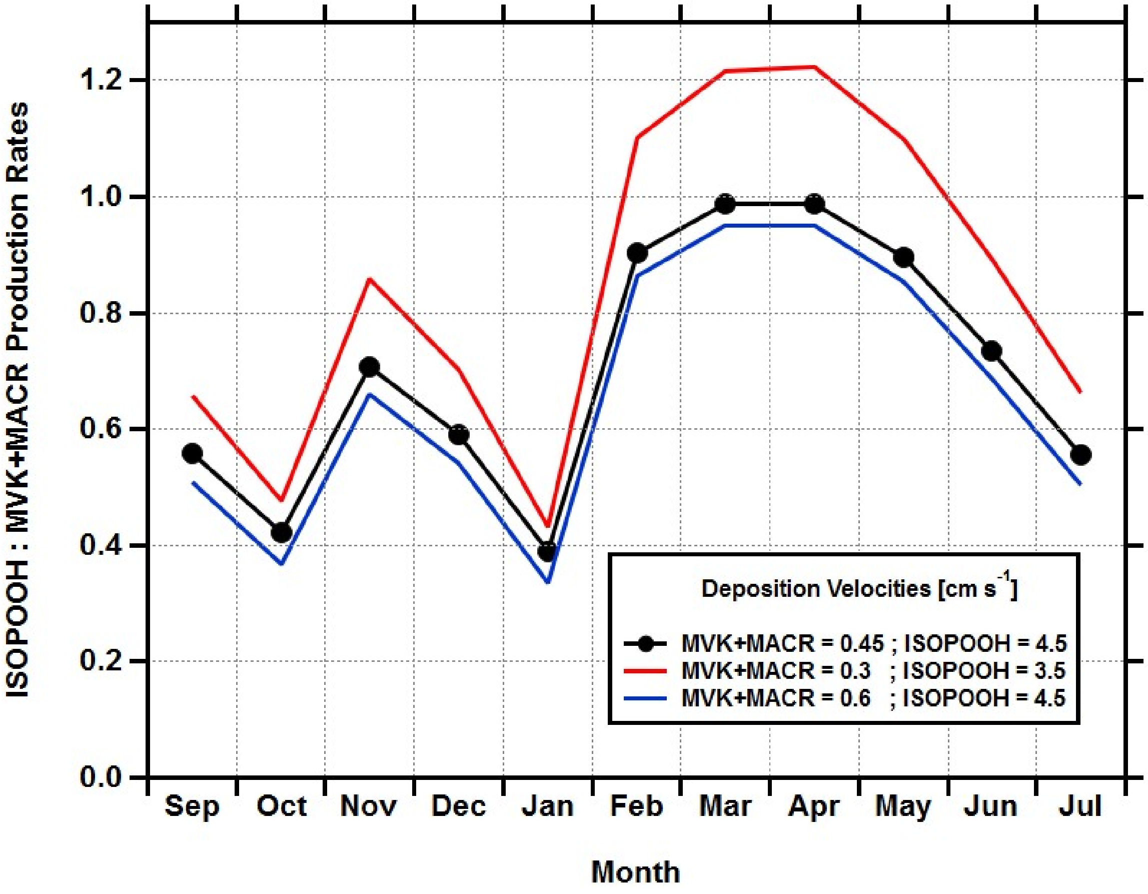

Figure S13. Concentration ratios of ISOPOOH / (MVK+MACR) were calculated following Eq. (1) and then converted to production ratios by multiplying by *x* calculated from Eq. (13). In each case the calculation of *x* considered the change in deposition velocities.

Figure S14 shows how the uncertainty in deposition velocities feeds through to the modelled reactive loss of ISOPOO to the four major oxidation pathways. Panel A, shows the scenario presented in figure 5A of the main manuscript, where the $V_{d(s)}$ for ISOPOOH and MVK+MACR are set ad 4.5 cm s^{-1} and 0.45 cm s^{-1}, respectively. Panel B, shows how the production ratios would change if the deposition velocity for MVK+MACR is increased to 0.6 cm s^{-1} to match the upper limit of values presented in the deposition scheme of Zhang et al. (30). Finally, panel C, shows a scenario where the $V_{d(s)}$ for MVK+MACR is reduced to the lower limit of 0.3 cm s^{-1} and the ISOPOOH deposition velocity is reduced to 3.5 cm s^{-1}, which would be equivalent to an R_c of approximately 6.5 s m^{-1}.

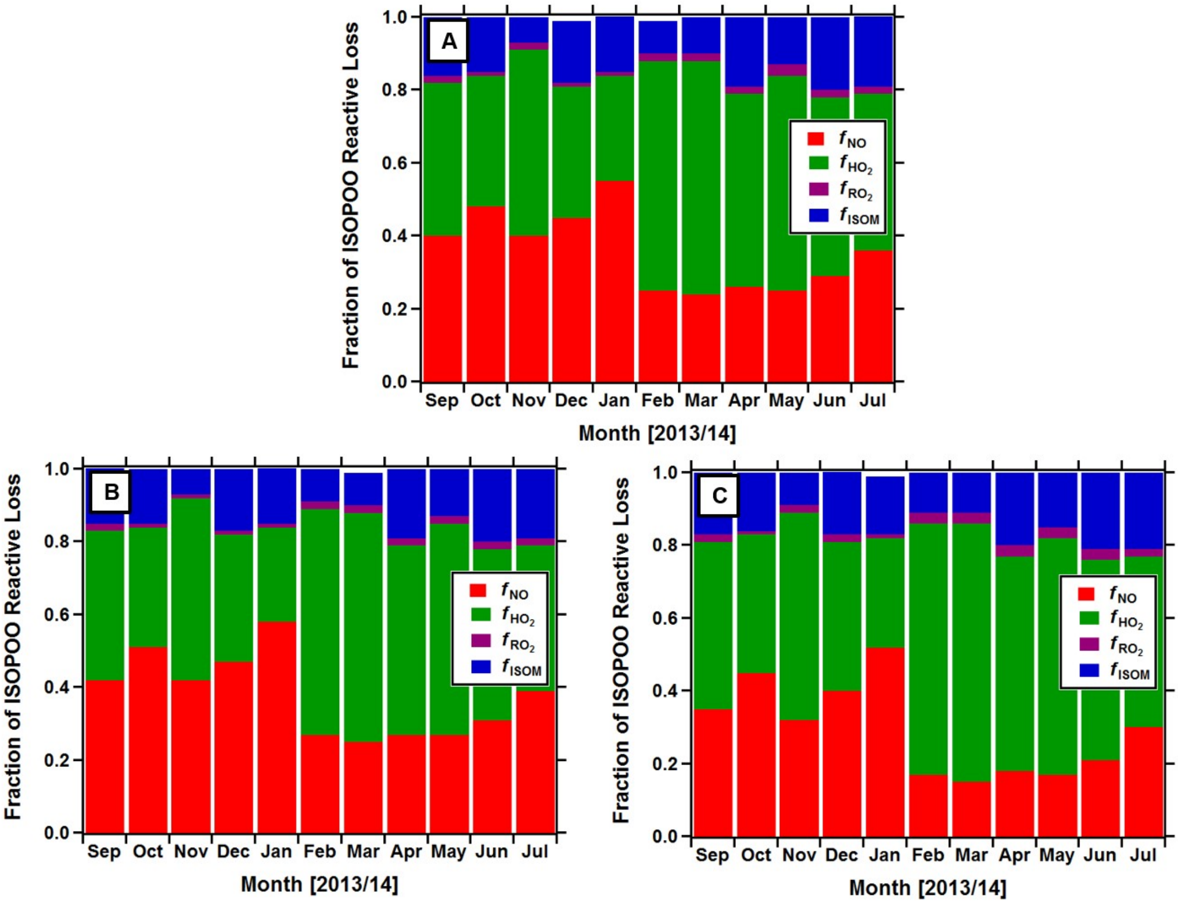

Figure S14 shows the fraction of ISOPOO reactive loss via the NO, HO_2, RO_2 and isomerisation pathways derived when the ISOPOOH and MVK+MACR deposition velocities are set to 4.5 cm s^{-1} and 0.45 cm s^{-1} respectively (Panel A). Panel B, shows how the chemical break down is changed if the MVK+MACR deposition velocity is increased to 0.6 cm s^{-1} and Panel C shows the impact of reducing the ISOPOOH and MVK+MACR deposition velocities to 3.5 and 0.3 cm s^{-1}, respectively.

The two extreme scenarios presented change the fraction of ISOPOO reactive loss expected for the NO pathway from an average of 36% for scenario A, to 38% for scenario B and 29% for scenario C. For HO_2, the average loss changes from 48% for scenario A, to 46% and 52% for scenarios B and C, respectively. Importantly, because the uncertainty in deposition velocities is systematic between months, the seasonal pattern in reactive loss remains the same with each scenario. The results are summarised for each month, together with the predicted NO concentration from the box modelling and are shown in Table S5.

Table S5 Fraction of ISOPOO reactive loss to the NO, HO2, RO2 and isomeristion chemical pathways and NO concentrations predicted by the MCM box modelling for the ISOPOOH/MVK+MACR production ratios calculated from Equation 1 and 2 of the main manuscript. Figures shown in bold are for an ISOPOOH and MVK+MACR $V_{d(s)}$ of 4.5 cm s^{-1} and

0.45 cm s^{-1}, respectively. Also shown are the modelling results based on production ratios for ISOPOOH and MVK+MACR $V_{d(s)}$ of 3.5 cm s^{-1} and 0.3 cm s^{-1} (+) and 4.5 cm s^{-1} and 0.6 cm s^{-1}, respectively (-).

		fNO	fHO2	fRO2	fISOM	NO concentration [pptv]
Sep		**0.40**	**0.42**	**0.02**	**0.16**	**104**
	+	0.35	0.46	0.02	0.17	86
	-	0.41	0.41	0.02	0.16	110
Oct		**0.48**	**0.36**	**0.01**	**0.15**	**145**
	+	0.44	0.39	0.01	0.16	127
	-	0.49	0.34	0.01	0.15	152
Nov		**0.40**	**0.51**	**0.02**	**0.07**	68
	+	0.32	0.57	0.02	0.09	52
	-	0.42	0.50	0.01	0.07	74
Dec		**0.45**	**0.36**	**0.01**	**0.17**	**103**
	+	0.39	0.41	0.02	0.18	85
	-	0.47	0.35	0.01	0.17	110
Jan		**0.55**	**0.29**	**0.01**	**0.16**	**139**
	+	0.50	0.32	0.01	0.16	122
	-	0.56	0.27	0.01	0.16	146
Feb		**0.25**	**0.63**	**0.02**	**0.09**	**34**
	+	0.17	0.69	0.03	0.10	22
	-	0.28	0.61	0.02	0.09	39
Mar		**0.24**	**0.64**	**0.02**	**0.10**	**32**
	+	0.16	0.70	0.03	0.11	20
	-	0.27	0.62	0.02	0.09	37
Apr		**0.26**	**0.53**	**0.02**	**0.19**	**43**
	+	0.19	0.58	0.03	0.20	29
	-	0.29	0.51	0.02	0.19	48
May		**0.25**	**0.59**	**0.03**	**0.13**	**38**
	+	0.18	0.65	0.03	0.15	25
	-	0.28	0.57	0.02	0.13	43
Jun		**0.29**	**0.49**	**0.02**	**0.20**	**48**
	+	0.22	0.54	0.03	0.21	34
	-	0.31	0.47	0.02	0.19	54
Jul		**0.36**	**0.43**	**0.02**	**0.20**	**65**
	+	0.29	0.48	0.02	0.21	50
	-	0.38	0.41	0.02	0.19	71

There are, however, several scenarios in which the uncertainty could become random rather than systematic. For example, if the conversion efficiency of ISOPOOH to MVK+MACR varies over time;

if ISOPOOH reacts increasingly with the long Teflon inlet lines as walls become coated with dust and organic films; if ISOPOOH and MVK+MACR show differing time-lags within the sample setup; or if the canopy resistance of either species were to change over time. These, are all potentially very large sources of uncertainty which we are unable to quantify retrospectively. Therefore, the uncertainties presented above should be viewed as a lower limit. Nonetheless, the close relationship between our derived production ratios and markers of biomass burning shown in Figure 3, provide at least a qualitative assessment of our approach and demonstrate an adherence to current theory.

6.3 Friction velocity threshold

Within our study we applied a friction velocity filter to the observed deposition velocities and removed those measurements obtained when $u_* < 0.3$ m s^{-1}. In order to ensure that the reported seasonal trend in the production ratio of ISOPOOH to MVK+MACR was not influenced by our choice of threshold we repeated the analysis over a range of thresholds between 0.15 m s^{-1} and 0.35 m s^{-1}. Figure S15 shows the resulting seasonal trends in the ISOPOOH to MVK+MACR production ratio and indicates it to be robust over the tested range.

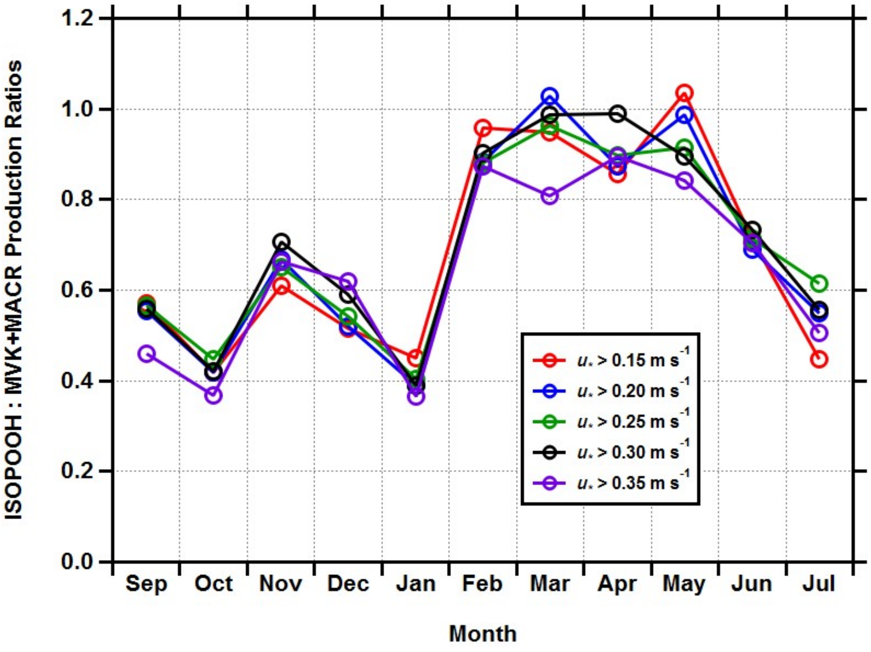

Figure S15. The seasonal trend in ISOPOOH to MVK+MACR production ratios calculated from flux measurements filtered by differing thresholds of the friction velocity, u_*.

7. Identifying periods of anthropogenic influence

In general terms the ZF2 site in the Cuieiras Reserve represents an ideal site to study isoprene oxidation chemistry. The combination of prevailing easterly wind direction, typically low wind speeds and distance from primary urban anthropogenic emission sources provides a low NO_x environment from which the effects of anthropogenic pollution can be benchmarked. However, emissions from biomass burning and occasionally plumes from Manaus reach the measurement site. In order to investigate periods when anthropogenic pollution was present at the ZF2 site, air mass back trajectories were calculated using the HYSPLIT (Hybrid Single Particle Lagrangian Integrated Trajectory) model (Draxler and Rolph, 2008). HYSPLIT was run at 3 hour release intervals starting at a height of 10 m from the ZF2 site and propagated backwards in time for the preceding 96 hours to cover the period of September 2013 to July 2014.

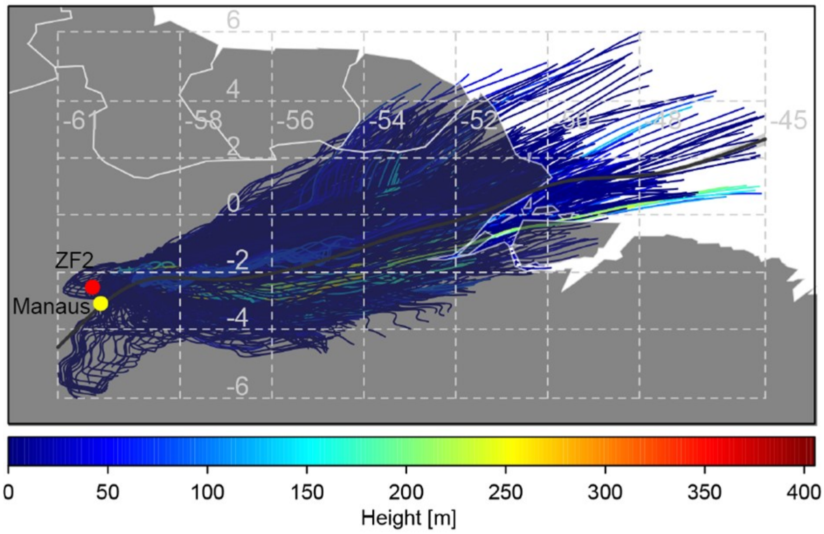

Figure S16. Plot showing all and the average (solid black line) of calculated back trajectories using the HYSPLIT model with the air mass height (m) within the boundary layer (colour bar), the measurement site (ZF2, red dot), Manaus (yellow dot).

Figure S16 shows that the air mass back trajectories were typically limited to the area to the north east of the site, with very occasional southerly observed in October 2013. The air parcels remained within the boundary layer and typically passed over large areas of forest with some back trajectories reaching as far as the Atlantic Ocean. Figure S17 shows the land cover types for the wider region at a resolution of 1 km^2 per pixel (Eva et al., 2003). Land cover maps may underestimate or overestimate land cover classes over fragmented areas depending on the spatial organisation of the respective class, but on a continental scale can provide representative land cover estimates. Most of the area is covered by lowland evergreen tropical forest with some areas of freshwater flooded tropical forest and flooded savannah along the Amazon River. This area has limited land transport connectivity, so the river provides the main transport route for human communities. This is reflected by the areas of mosaic agriculture and degraded forests with some intensive agriculture and patches of shrub savannah with little or sparse vegetation along the river banks and towards the Amazon Delta. The largest urbanised areas along the river are Manaus (1.8 million), Santarém (0.2 million), and Macapá (0.4 million).

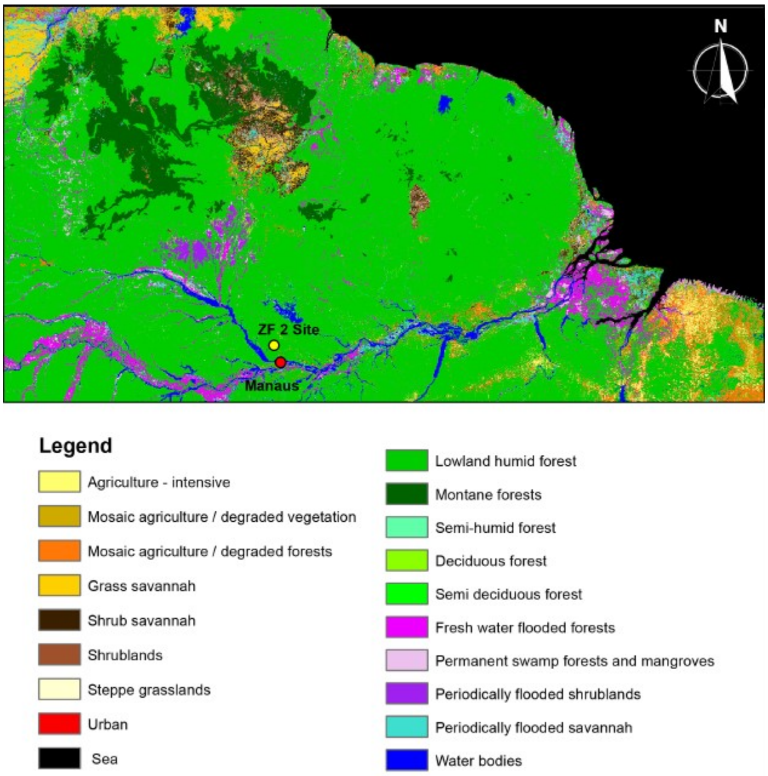

Figure S17. A map of north western South America showing land cover types where 1 pixel represents 1 km^2 with references to the measurement site (ZF2, yellow dot) and Manaus (red dot). Categories are given in the legend. Section reproduced from(51).

The back trajectories were analysed in relation to the measured concentrations of BC at the ZF2 site to confirm periods of possible anthropogenic influences. The dry season is the peak period for biomass burning with increased slash and burn activities associated with the mosaic agricultural systems identified on the land cover map. This was reflected by increased BC concentrations during September and October 2013 which extended on occasion through November, December 2013, and January 2014.

The following example periods were identified to have a strong anthropogenic influence based on their back trajectory and BC concentration: 17 - 20 September, 22 – 25 September, 23-28 October, 5 - 12 December, 2013, 1 - 4 January, 18-22 January 2014 and a number of individual days in February to May 2014. The back trajectories for each of these specific periods are shown in Fig S18. There were periods where back trajectories indicated a southerly course before reaching the site, but it is clear that at the ZF2 site there was typically no, or very little, contamination from the Manaus plume on those days. The VOC compounds detected at *m/z* 69 (isoprene) and 71 (MVK+MACR+ISOPOOH) have relatively short atmospheric lifetimes and showed no anomalies in mixing ratios during these periods, suggesting that measurements of the selected *m/z* at this site were unaffected by other compounds associated with anthropogenic pollution (e.g. furan).

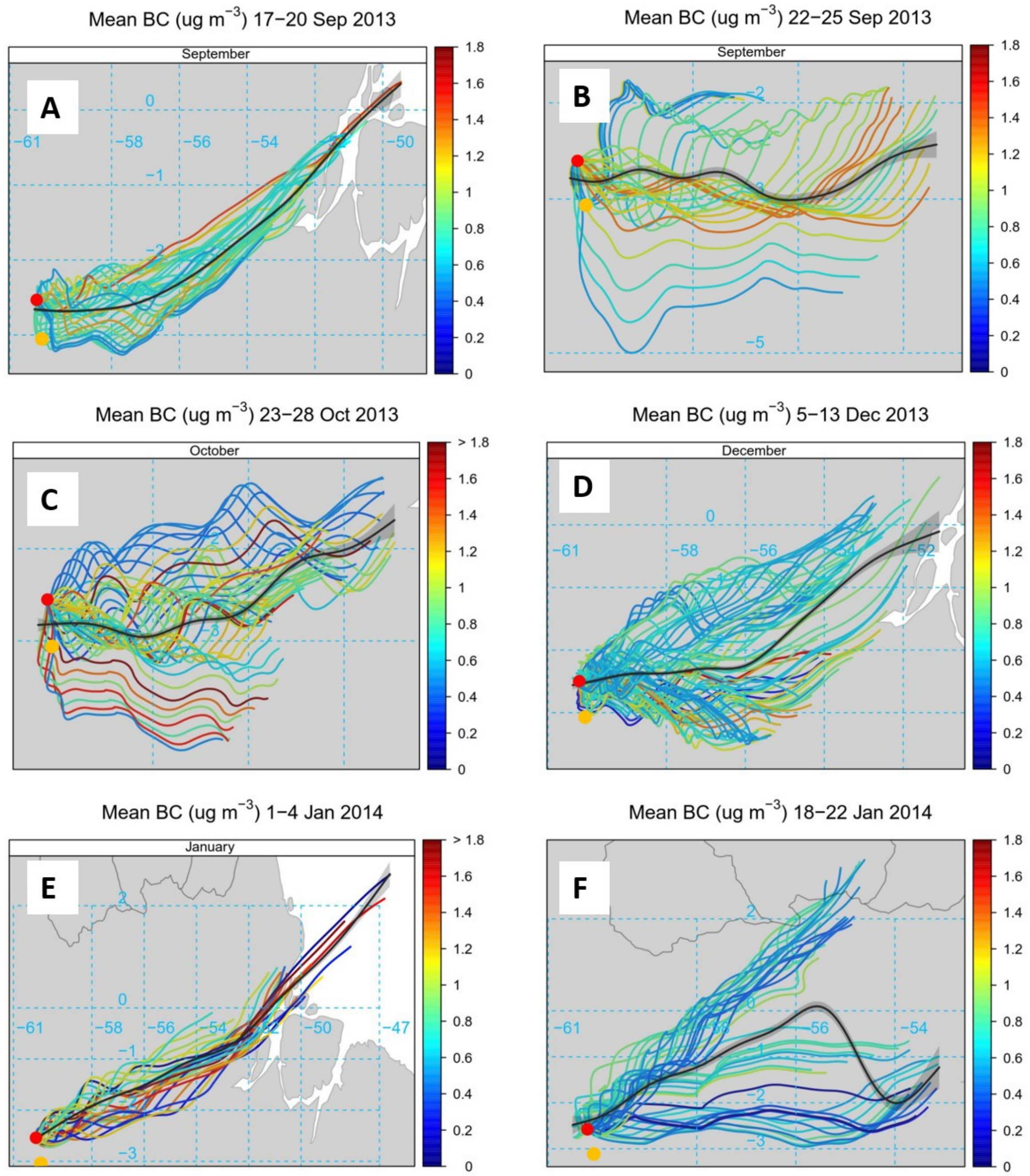

Figure S18 Air mass back trajectories for example periods in September (Panels A and B), October (Panel C), December (Panel D) and January (Panels E and F) when the concentration of black carbon indicated possible anthropogenic influences. The ZF2 measurement site and city of Manaus are highlighted with a red and orange circle, respectively.

8. Comparison of Acetonitrile and MODIS active fire count data

In order to confirm that our measurements of acetonitrile were a suitable marker of biomass burning we compared the monthly acetonitrile concentrations to number and brightness (surface temperature, K) of terrestrial fire events observed by the Terra MODIS satellite along calculated back trajectories. The comparison was carried out in the R statistical environment (R Core Team, 2019) using the sf package of Pebesma (2018)(52). Trajectories for the period 28th August 2013 to 31st July 2014 were calculated using the HYSPLIT model(53). Four back trajectories were calculated each day starting at 00, 06, 12, 18 hrs and travelling back over the previous 24 hours. Individual fire events that occurred within a 5 km radius of each trajectory were included in the analysis. The back trajectory was restricted to 24 hrs because beyond this time it is unlikely that NO would remain elevated within the fire plume. The number of fires counted and the average brightness (calculated as the brightness of the fire pixel minus the brightness of the background pixel) were recorded for only those days where PTR-MS measurements were recorded. Figure S19 shows the comparison between acetonitrile concentrations, fire counts and brightness. It is clear that biomass burning events only take place between September and January 2013,with no more than 3 per month observed between February and July 2014. The concentrations of acetonitrile between February and July ranged between 0.16 and 0.12 ppb and can therefore be considered background levels. Between September and January acetonitrile ranged between 0.26 and 0.29 ppb but correlated poorly with the number of fire counts, because the fire counts do not account for the size of the fire. A further comparison with the fire brightness, a metric of fire intensity shows a much more similar temporal trend to that of acetonitrile and provides further supporting evidence that the observed acetonitrile is likely to originate from biomass burning activities within the Amazon basin.

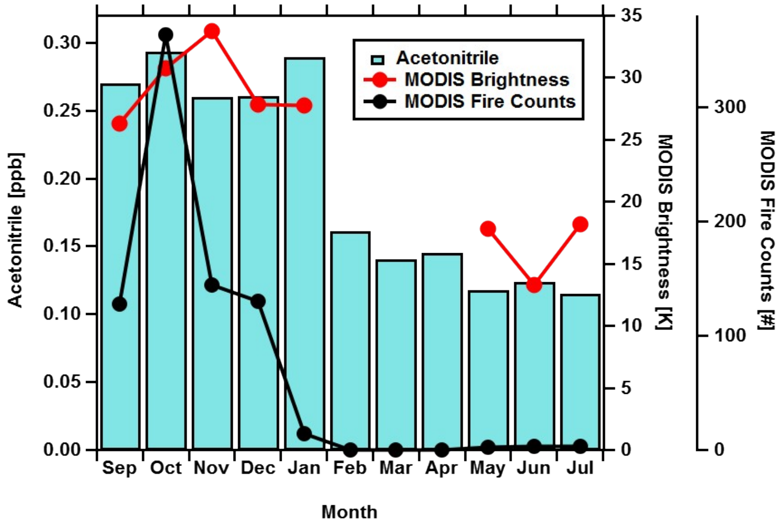

Figure S19. Measured monthly average acetonitrile concentrations at the ZF2 measurement site and the number and intensity (Brightness, K) of fires observed within a 5 km radius of daily calculated back trajectories between September 2013 and July 2014.

7. References

1. Leaf Area Index (TERRA/MODIS). NASA Earth Observations2014.
2. Instituto Nacional de Meteorologia. Brasília, Federal District, Brazil2014 [updated May 4].
3. Eltahir EAB, Bras RL. Precipitation recycling. Reviews of Geophysics. 1996;34(3):367-78.
4. Poveda CANGOOJAMRFG. Characteristics of Amazonian Climate: Main Features. Amazonia and Global Change.
5. Tanaka LMdS, Satyamurty P, Machado LAT. Diurnal variation of precipitation in central Amazon Basin. International Journal of Climatology. 2014;34(13):3574-84.
6. Araújo AC, Nobre AD, Kruijt B, Elbers JA, Dallarosa R, Stefani P, et al. Comparative measurements of carbon dioxide fluxes from two nearby towers in a central Amazonian rainforest: The Manaus LBA site. Journal of Geophysical Research: Atmospheres. 2002;107(D20):LBA 58-1-LBA -20.
7. Ribeiro JELdS, Hopkins MJG, Vicentini A. Flora da Reserva Ducke : guia de identificação das plantas vasculares de uma floresta de terra-firme na Amazônia Central: Manaus : INPA; 1999.
8. Andreae MO, Artaxo P, Brandao C, Carswell FE, Ciccioli P, da Costa AL, et al. Biogeochemical cycling of carbon, water, energy, trace gases, and aerosols in Amazonia: The LBA-EUSTACH experiments. Journal of Geophysical Research-Atmospheres. 2002;107(D20).
9. Pitman NCA, Terborgh JW, Silman MR, Núñez V P, Neill DA, Cerón CE, et al. DOMINANCE AND DISTRIBUTION OF TREE SPECIES IN UPPER AMAZONIAN TERRA FIRME FORESTS. Ecology. 2001;82(8):2101-17.
10. Santos F, Longo K, Guenther A, Kim S, Gu D, Oram D, et al. Biomass burning emission disturbances of isoprene oxidation in a tropical forest. Atmos Chem Phys. 2018;18(17):12715-34.
11. Rivera-Rios JC, Nguyen TB, Crounse JD, Jud W, St Clair JM, Mikoviny T, et al. Conversion of hydroperoxides to carbonyls in field and laboratory instrumentation: Observational bias in diagnosing pristine versus anthropogenically controlled atmospheric chemistry. Geophysical Research Letters. 2014;41(23):8645-51.
12. Statistical Methods in Water Resources. New York: Elsevier; 1992.
13. Clarke JU. Evaluation of censored data methods to allow statistical comparisons among very small samples with below detection limit observations. Environ Sci Technol. 1998;32:177–83.
14. Inomata S, Tanimoto H, Kameyama S, Tsunogai U, Irie H, Kanaya Y, et al. Technical Note: Determination of formaldehyde mixing ratios in air with PTR-MS: laboratory experiments and field measurements. Atmos Chem Phys. 2008;8(2):273-84.
15. Kameyama S, Tanimoto H, Inomata S, Tsunogai U, Ooki A, Yokouchi Y, et al. Equilibrator Inlet-Proton Transfer Reaction-Mass Spectrometry (EI-PTR-MS) for Sensitive, High-Resolution Measurement of Dimethyl Sulfide Dissolved in Seawater. Analytical Chemistry. 2009;81(21):9021-6.
16. Kameyama S, Tanimoto H, Inomata S, Tsunogai U, Ooki A, Takeda S, et al. High-resolution measurement of multiple volatile organic compounds dissolved in seawater using equilibrator inlet–proton transfer reaction-mass spectrometry (EI–PTR-MS). Marine Chemistry. 2010;122(1):59-73.
17. Kameyama S, Yoshida S, Tanimoto H, Inomata S, Suzuki K, Yoshikawa-Inoue H. High-resolution observations of dissolved isoprene in surface seawater in the Southern Ocean during austral summer 2010–2011. Journal of Oceanography. 2014;70(3):225-39.
18. Langford B, Acton W, Ammann C, Valach A, Nemitz E. Eddy-covariance data with low signal-to-noise ratio: time-lag determination, uncertainties and limit of detection. Atmospheric Measurement Techniques. 2015;8(10):4197-213.
19. Petzold A, Schloesser H, Sheridan PJ, Arnott WP, Ogren JA, Virkkula A. Evaluation of Multiangle Absorption Photometry for Measuring Aerosol Light Absorption. Aerosol Sci Technol. 2005;39(1):40-51.
20. Müller T, Laborde M, Kassell G, Wiedensohler A. Design and performance of a three-wavelength LED-based total scatter and backscatter integrating nephelometer. Atmos Meas Tech. 2011;4(6):1291-303.
21. Tuch TM, Haudek A, Müller T, Nowak A, Wex H, Wiedensohler A. Design and performance of an automatic regenerating adsorption aerosol dryer for continuous operation at monitoring sites. Atmos Meas Tech. 2009;2(2):417-22.

22. A. Sedlacek CS, E. Andrews and S. Springston. Atmospheric Radiation Measurement (ARM) user facility. 2014, updated hourly. Aethalometer (AOSAETH1SPOT). 2014-01-21 to 2015-12-01, ARM Mobile Facility (MAO) Manacapuru, Amazonas, Brazil; MAOS (S1). Data set accessed 2019-05-24 at http://dx.doi.org/10.5439/1095582. ARM Data Center: ARM Data Center; 2019.

23. Springston S. Nitrogen Oxides Monitor (AOSNOX). 2014-01-19 to 2015-12-01, ARM Mobile Facility (MAO) Manacapuru, Amazonas, Brazil; MAOS (S1). Data set accessed 2019-05-24 at http://dx.doi.org/10.5439/1095582. ARM Data Center: ARM Data Center; 2019.

24. Langford B, Cash J, Acton WJF, Valach AC, Hewitt CN, Fares S, et al. Isoprene emission potentials from European oak forests derived from canopy flux measurements: an assessment of uncertainties and inter-algorithm variability. Biogeosciences. 2017;14(23):5571-94.

25. Guenther A, Karl T, Harley P, Wiedinmyer C, Palmer PI, Geron C. Estimates of global terrestrial isoprene emissions using MEGAN (Model of Emissions of Gases and Aerosols from Nature). Atmospheric Chemistry and Physics. 2006;6:3181-210.

26. Guenther AB, Jiang X, Heald CL, Sakulyanontvittaya T, Duhl T, Emmons LK, et al. The Model of Emissions of Gases and Aerosols from Nature version 2.1 (MEGAN2.1): an extended and updated framework for modeling biogenic emissions. Geoscientific Model Development. 2012;5(6):1471-92.

27. Massman WJ, Lee X. Eddy covariance flux corrections and uncertainties in long-term studies of carbon and energy exchanges. Agricultural and Forest Meteorology. 2002;113(1-4):121-44.

28. Nguyen TB, Crounse JD, Teng AP, Clair JMS, Paulot F, Wolfe GM, et al. Rapid deposition of oxidized biogenic compounds to a temperate forest. Proceedings of the National Academy of Sciences of the United States of America. 2015;112(5):E392-E401.

29. Iraci LT, Baker BM, Tyndall GS, Orlando JJ. Measurements of the Henry's Law Coefficients of 2-Methyl-3-buten-2-ol, Methacrolein, and Methylvinyl Ketone. Journal of Atmospheric Chemistry. 1999;33(3):321-30.

30. Zhang L, Brook JR, Vet R. A revised parameterization for gaseous dry deposition in air-quality models. Atmos Chem Phys. 2003;3(6):2067-82.

31. Zhang L, Moran MD, Makar PA, Brook JR, Gong S. Modelling gaseous dry deposition in AURAMS: a unified regional air-quality modelling system. Atmospheric Environment. 2002;36(3):537-60.

32. Canaval E, Millet DB, Zimmer I, Nosenko T, Georgii E, Partoll EM, et al. Rapid conversion of isoprene photooxidation products in terrestrial plants. Communications Earth & Environment. 2020;1(1):44.

33. Jardine KJ, Monson RK, Abrell L, Saleska SR, Arneth A, Jardine A, et al. Within-plant isoprene oxidation confirmed by direct emissions of oxidation products methyl vinyl ketone and methacrolein. Global Change Biology. 2012;18(3):973-84.

34. Liu YJ, Brito J, Dorris MR, Rivera-Rios JC, Seco R, Bates KH, et al. Isoprene photochemistry over the Amazon rainforest (vol 113, pg 6125, 2016). Proceedings of the National Academy of Sciences of the United States of America. 2016;113(51):E8358-E.

35. Torres AL, Buchan H. Tropospheric nitric oxide measurements over the Amazon Basin. Journal of Geophysical Research: Atmospheres. 1988;93(D2):1396-406.

36. Bakwin PS, Wofsy SC, Fan SM, Keller M, Trumbore SE, Dacosta JM. EMISSION OF NITRIC-OXIDE (NO) FROM TROPICAL FOREST SOILS AND EXCHANGE OF NO BETWEEN THE FOREST CANOPY AND ATMOSPHERIC BOUNDARY-LAYERS. Journal of Geophysical Research-Atmospheres. 1990;95(D10):16755-64.

37. Liu YJ, Seco R, Kim S, Guenther AB, Goldstein AH, Keutsch FN, et al. Isoprene photo-oxidation products quantify the effect of pollution on hydroxyl radicals over Amazonia. Science Advances. 2018;4(4).

38. Vilà-Guerau de Arellano J, Patton EG, Karl T, van den Dries K, Barth MC, Orlando JJ. The role of boundary layer dynamics on the diurnal evolution of isoprene and the hydroxyl radical over tropical forests. Journal of Geophysical Research: Atmospheres. 2011;116(D7).

39. Rohrer F, Lu K, Hofzumahaus A, Bohn B, Brauers T, Chang C-C, et al. Maximum efficiency in the hydroxyl-radical-based self-cleansing of the troposphere. Nature Geoscience. 2014;7:559.

40. Jenkin ME, Young JC, Rickard AR. The MCM v3.3.1 degradation scheme for isoprene. Atmospheric Chemistry and Physics. 2015;15(20):11433-59.

41. Paulot F, Crounse JD, Kjaergaard HG, Kürten A, St. Clair JM, Seinfeld JH, et al. Unexpected Epoxide Formation in the Gas-Phase Photooxidation of Isoprene. Science. 2009;325(5941):730-3.

42. Hudman RC, Moore NE, Mebust AK, Martin RV, Russell AR, Valin LC, et al. Steps towards a mechanistic model of global soil nitric oxide emissions: implementation and space based-constraints. Atmos Chem Phys. 2012;12(16):7779-95.

43. Giglio L, Randerson JT, van der Werf GR. Analysis of daily, monthly, and annual burned area using the fourth-generation global fire emissions database (GFED4). Journal of Geophysical Research: Biogeosciences. 2013;118(1):317-28.

44. Marais EA, Jacob DJ, Jimenez JL, Campuzano-Jost P, Day DA, Hu W, et al. Aqueous-phase mechanism for secondary organic aerosol formation from isoprene: application to the southeast United States and co-benefit of SO2 emission controls. Atmos Chem Phys. 2016;16(3):1603-18.

45. Mao J, Paulot F, Jacob DJ, Cohen RC, Crounse JD, Wennberg PO, et al. Ozone and organic nitrates over the eastern United States: Sensitivity to isoprene chemistry. Journal of Geophysical Research: Atmospheres. 2013;118(19):11,256-11,68.

46. Marais EA, Jacob DJ, Turner JR, Mickley LJ. Evidence of 1991–2013 decrease of biogenic secondary organic aerosol in response to SO2 emission controls. Environmental Research Letters. 2017;12(5):054018.

47. Pye HOT, Chan AWH, Barkley MP, Seinfeld JH. Global modeling of organic aerosol: the importance of reactive nitrogen (NO_x and NO₃). Atmos Chem Phys. 2010;10(22):11261-76.

48. Newland MJ, Bryant DJ, Dunmore RE, Bannan TJ, Acton WJF, Langford B, et al. Rainforest-like Atmospheric Chemistry in a Polluted Megacity. Atmos Chem Phys Discuss. 2020;2020:1-18.

49. Shrivastava M, Andreae MO, Artaxo P, Barbosa HMJ, Berg LK, Brito J, et al. Urban pollution greatly enhances formation of natural aerosols over the Amazon rainforest. Nature Communications. 2019;10(1):1046.

50. Barkley MP, Palmer PI, De Smedt I, Karl T, Guenther A, Van Roozendael M. Regulated large-scale annual shutdown of Amazonian isoprene emissions? Geophysical Research Letters. 2009;36.

51. The Land Cover Map for South America in the Year 2000 from the GLC2000 database. Brussels: European Commision Joint Research Centre, 2003.

52. Pebesma E. Simple Features for R: Standardized Support for Spatial Vector Data. The R Journal. 2018;10(1):439--46.

53. Stein AF, Draxler RR, Rolph GD, Stunder BJB, Cohen MD, Ngan F. NOAA's HYSPLIT Atmospheric Transport and Dispersion Modeling System. Bulletin of the American Meteorological Society. 2015;96(12):2059-77.